
# BRNO UNIVERSITY OF TECHNOLOGY
VYSOKÉ UČENÍ TECHNICKÉ V BRNĚ

## FACULTY OF MECHANICAL ENGINEERING
FAKULTA STROJNÍHO INŽENÝRSTVÍ

## INSTITUTE OF PHYSICAL ENGINEERING
ÚSTAV FYZIKÁLNÍHO INŽENÝRSTVÍ


# PLASMONIC ANTENNAS FOR HIGH WAVELENGTHS
PLAZMONICKÉ ANTÉNY PRO VYSOKÉ VLNOVÉ DÉLKY

**MASTER'S THESIS**
DIPLOMOVÁ PRÁCE


**AUTHOR** — **Bc. Adam Beneš**
AUTOR PRÁCE

**SUPERVISOR** — **Mgr. Vlastimil Křápek, Ph.D.**
VEDOUCÍ PRÁCE



**BRNO 2021**

BRNO UNIVERSITY OF TECHNOLOGY
FACULTY OF MECHANICAL ENGINEERING

# Assignment Master's Thesis

| | |
|---|---|
| Institut: | Institute of Physical Engineering |
| Student: | **Bc. Adam Beneš** |
| Degree programm: | Physical Engineering and Nanotechnology |
| Branch: | no specialisation |
| Supervisor: | **Mgr. Vlastimil Křápek, Ph.D.** |
| Academic year: | 2020/21 |

As provided for by the Act No. 111/98 Coll. on higher education institutions and the BUT Study and Examination Regulations, the director of the Institute hereby assigns the following topic of Master's Thesis:

## Plasmonic antennas for high wavelengths

**Brief Description:**

Plasmonic antennas are metallic nanostructures or microstructures utilized for a focusation and enhancement of the electromagnetic field. Their properties are related to the excitation of surface plasmon polaritons whose near field is not restricted by the diffraction limit. Traditionally, plasmonic antennas operate in the visible, ultraviolet, or near infrared spectral range. It is however possible to utilize them also in the microwave, terahertz, or far infrared spectral range, either by scaling their dimensions, or by employing low–plasma–frequency materials.
The thesis will address the properties of plasmonic antennas supporting localized plasmon resonances at high wavelengths, in particular in relation to applications in plasmon–enhanced high–frequency electron paramagnetic resonance. It can focus on theory (simulations of antennas, assessment of the suitability of the antennas for specific applications, optimized design), experiment (fabrication or characterization of the antennas) or both.

**Master's Thesis goals:**

To study the properties of plasmonic antennas for high wavelengths.
To design the antennas for enhanced high–frequency electron paramagnetic resonance.

**Recommended bibliography:**

WEIL, John A. a James R. BOLTON. Electron paramagnetic resonance: elementary theory and practical applications. 2nd ed. Hoboken, N.J.: Wiley-Interscience, c2007. ISBN 978-0-471-75496-1.

SHTIRBERG, Lazar, Ygal TWIG, Ekaterina DIKAROV, Revital HALEVY, Michael LEVIT a Aharon BLANK. High-sensitivity Q-band electron spin resonance imaging system with submicron resolution. Review of Scientific Instruments [online]. 2011, 82(4), 043708 [cit. 2020-10-24]. ISSN 0034-6748. Dostupné z: doi:10.1063/1.3581226

BLANK, Aharon, Ekaterina SUHOVOY, Revital HALEVY, Lazar SHTIRBERG a Wolfgang HARNEIT. ESR imaging in solid phase down to sub-micron resolution: methodology and applications. Physical Chemistry Chemical Physics [online]. 2009, 11(31), 6689 [cit. 2020-10-24]. ISSN 1463-9076. Dostupné z: doi:10.1039/b905943a

TWIG, Ygal, Ekaterina DIKAROV, Wayne D. HUTCHISON a Aharon BLANK. Note: High sensitivity pulsed electron spin resonance spectroscopy with induction detection. Review of Scientific Instruments [online]. 2011, 82(7), 076105 [cit. 2020-10-24]. ISSN 0034-6748. Dostupné z: doi:10.1063/1.3611003

RECHKEMMER, Yvonne, Julia E. FISCHER, Raphael MARX, et al. Comprehensive Spectroscopic Determination of the Crystal Field Splitting in an Erbium Single-Ion Magnet. Journal of the American Chemical Society [online]. 2015, 137(40), 13114-13120 [cit. 2020-10-24]. ISSN 0002-7863. Dostupné z: doi:10.1021/jacs.5b08344

TAKAHASHI, Hideyuki, Eiji OHMICHI a Hitoshi OHTA. Mechanical detection of electron spin resonance beyond 1 THz. Applied Physics Letters [online]. 2015, 107(18) [cit. 2020-10-24]. ISSN 0003-6951. Dostupné z: doi:10.1063/1.4935204

MAIER, Stefan A. Plasmonics: Fundamentals and Applications [online]. New York, NY: Springer US, 2007 [cit. 2020-10-24]. ISBN 978-0-387-33150-8. Dostupné z: doi:10.1007/0-387-37825-1

Deadline for submission Master's Thesis is given by the Schedule of the Academic year 2020/21

In Brno,

L. S.

prof. RNDr. Tomáš Šikola, CSc.
Director of the Institute

doc. Ing. Jaroslav Katolický, Ph.D.
FME dean

**Summary**
This master's thesis deals with properties of plasmonic antennas for high wavelengths. Resonant properties of individual antennas as well as periodical arrays of the antennas are described. The work utilizes numerical simulations of magnetic field enhancement produced in the near field of antennas. This enhancement might increase a signal of high-frequency electron paramagnetic resonance (HFEPR). The average enhancement is quantified using antennas of various shapes. The author optimizes the shape of frequently used plasmonic antennas but designs new one as well. A significant part of the thesis also tries to distinguish phenomena that contribute to overall magnetic field enhancement while using double transmission HFEPR measurement setup.

**Abstrakt**
Tato diplomová práce se zabývá vlastnostmi plazmonických antén v oblasti vysokých vlnových délek. Důraz je kladen na popis rezonančních vlastností jednotlivých antén i antén uspořádaných do periodických polí. Těžiště práce spočívá v počítačovém modelování navýšení magnetického pole v blízkosti antén, které lze využít ve vysokofrekvenční elektronové paramagnetické rezonanci (HFEPR) k zesílení měřeného signálu. Autor se zabývá kvantifikací zesílení v anténách s odlišnou geometrií a navrhuje i geometrii vlastní. Značná část práce se také věnuje snaze rozlišit příspěvky k navýšení magnetického pole od různých zdrojů při měření HFEPR v uspořádání s dvojitou transmisí záření.

**Keywords**
plasmonic antennas, near field magnetic enhancement, HFEPR, FDTD simulations, THz frequency range

**Klíčová slova**
plazmonické antény, navýšení blízkého magnetického pole, HFEPR, FDTD simulace, THz frekvenční oblast

BENEŠ, A. *Plasmonic antennas for high wavelengths.* Brno: University of Technology, Faculty of Mechanical Engineering, Institute of Physical Engineering, 2021. 70 p. Supervisor Mgr. Vlastimil Křápek, Ph.D.

I honestly declare that I have created this work individually under supervision of Mgr. Vlastimil Křápek, Ph.D. and all literature and sources are listed in the dedicated part.

Bc. Adam Beneš

*I find impossible to mention all the people who helped me during my studies and I find it even harder to mention only few of them.*

Herewith I would like to express my gratitude to Mgr. Vlastimil Křápek, Ph.D. for his supervision, priceless suggestions and rigorous comments on the text of this thesis. I trully appreciate attitude of Ing. Martin Hrtoň who helped me to understand and use his semi-analytical model and frequently discussed the results with me. Part of this thesis could not be done without support of Prof. Dr. Joris van Slageren and Dr. Lorenzo Tesi; therefore, many thanks also to them.

Finally, this thesis would never see the light of day without the immense support and patience of my family. Special thanks goes to Jana and David for comments on the text and for sharing problems of this thesis with me, although they are not physicists.

Bc. Adam Beneš

# Contents

# Introduction

Plasmonics is one of the leading branches of nanophotonics. It studies the interaction of electromagnetic waves (photons) with conduction electrons at metal-dielectric interfaces. When proper conditions are met, coupling of photons with electrons may lead to the creation of a quasi-particle referred to as the surface plasmon polariton (SPP). These quasiparticles can be very often described simply as electromagnetic waves. Their wavelengths are not restricted as long as they propagate along infinite metal-dielectric interface. However, when the interface becomes spatially limited, standing SPP waves are formed with discrete values of the wavelength. This phenomenon is analogous to standing wave patterns supported by a string. As the SPPs become spatially localized they are called localized surface plasmons (LSPs) and structures forming finite metal-dielectric are referred to as plasmonic antennas or plasmonic resonators.

Although the theoretical description of surface electromagnetic waves propagating along the interfaces was done more than a hundred years ago, plasmonics had to wait for its *renaissance* till the end of the 20th century. In that time, fabrication techniques became widely available. Rapid development of computational techniques enabling numerical prediction of properties brings another significant contribution to the plasmonic boom. So far, plasmonic applications cover Raman and infrared spectroscopy [1], fluorescence and luminescence enhancement [2], [3], hydrogen sensing [4] or even rapid colourimetric test devices [5]. This short enumeration confirms the enormous potential of plasmonics. Majority of these applications focuses on the visible or the infrared part of the spectrum and benefits from an enhancement of electric field in the vicinity of antennas. This thesis differs in both, it deals with properties of plasmonic antennas at THz frequencies and studies the possibility of magnetic field enhancement.

So-called terahertz region is a loosely defined part of the electromagnetic spectrum ranging from 100 GHz to 10 THz (30–3000 µm). The number of applications or scientific tools operating in this region remains very low. Historically, astronomy and space-related fields were leading the development of THz technologies [6]. In recent years instruments for molecular structure characterization were also developed [7]. Another widely used technique is electron paramagnetic resonance (EPR) spectroscopy which detects unpaired electrons. Development of superconducting magnets with fields exceeding 10 T pushed this technique to THz region, giving rise to so-called high-frequency electron paramagnetic resonance (HFEPR) [8]. Generally speaking, experiments in the THz region suffer from weak signal, since available sources of radiation exhibit low output power hardly exceeding tens of milliwatts [9]. In HFEPR the sam-

ple interacts with the magnetic component of the electromagnetic wave; therefore, its enhancement might significantly improve the sensitivity of the method.

The presented master's thesis focuses on numerical prediction of plasmonic antennas properties and magnetic field enhancement in their vicinity. Numerical simulations are performed using Finite-Difference in Time-Domain (FDTD) method. Chapter 1 provides the reader with the classical description of the electromagnetic field in the matter. Maxwell equations are supplemented by material and constitutive relations. The dielectric function of matter and the Drude model are also presented. Chapter 2 deals with two fundamental plasmonic excitations, SPP and LSP. The author derives resonant properties using a model of a spherical particle in an external electric field. Electric dipole radiation pattern is also shown. In Chapter 3 fundamentals of EPR spectroscopy are presented together with a short description of HFEPR setup at the University of Stuttgart. Zeeman effect and energy splitting are also described. Chapter 4 is devoted to a description of semi-analytical model employed to describe a complex plasmonic resonator utilized to enhance the magnetic field. Chapter 5 then gives a quick overview of numerical methods which can be used in calculations of plasmonic antennas properties. FDTD method is discussed in more details. Finally, Chapter 6 presents methods that have been used, shows and discusses results of the antennas geometry optimization process and magnetic field enhancement. The results are summarized in Conclusion.

# 1. Theory of electromagnetic field

In this chapter, the classical description of the electromagnetic field and its interaction with linear, isotropic and non-magnetic media will be shown. First, the Maxwell equations and constitutive relations are presented, then we show the dielectric function of materials and at the end of this chapter theoretical model describing the dielectric function of metals is derived. We will use the approach from [10].

## 1.1 Maxwell's equations in matter

Propagation and interaction such as absorption or scattering of electromagnetic waves in matter can be described without employing the quantum mechanics. The classical approach is based on four macroscopic equations named after James Clerk Maxwell. These equations were rewritten to the present form using vector formalism by Oliver Heaviside more than a hundred years ago [11]. We will write them down in differential form [12, p. 330].

$$\nabla \cdot \mathbf{D} = \rho_{\mathrm{f}}, \tag{1.1}$$

$$\nabla \cdot \mathbf{B} = 0, \tag{1.2}$$

$$\nabla \times \mathbf{E} = -\frac{\partial \mathbf{B}}{\partial t}, \tag{1.3}$$

$$\nabla \times \mathbf{H} = \mathbf{J}_{\mathrm{f}} + \frac{\partial \mathbf{D}}{\partial t}. \tag{1.4}$$

In these equations $\mathbf{E}$ is the electric field, $\mathbf{B}$ is the magnetic induction, $\rho_{\mathrm{f}}$ is the density of free charge, $\mathbf{J}_{\mathrm{f}}$ is the density of free current. These equations divide total charge and total current density into free and bounded parts. Alternatively, the current densities and the total charges could be divided into external and internal parts. The external quantities drive the system and the internal one respond to external goad [10, p. 7]. None of these approaches is more general than the other one. The bounded charge and current are related to the polarization of matter and are hidden to auxiliary field quantities $\mathbf{D}$ and $\mathbf{H}$, that are related to $\mathbf{E}$ and $\mathbf{B}$ via constitutive relations. Only free charge and current are then left as the sources of the auxiliary electric and magnetic field. As we treat a material which is under influence of electromagnetic radiation, there will be accumulation of charge and current which we can not directly control. It is more

eligible to include only these charges and currents we can control. Equations 1.1–1.4 have to be supplemented by the material relations linking together the field quantities **E** and **D**, **B** and **H**.

$$\mathbf{D} = \epsilon_0 \mathbf{E} + \mathbf{P}, \tag{1.5}$$

$$\mathbf{H} = \frac{1}{\mu_0}\mathbf{B} - \mathbf{M}, \tag{1.6}$$

where **P** is polarization field, **M** is magnetization field, $\epsilon_0$ and $\mu_0$ are the vacuum permitivity and permeability, respectively. Here we focus on nonmagnetic, linear and isotropic materials thus we do not need to consider a magnetic response represented by **M**. Electric dipole moment per unite volume induced in material with the electric field is decribed by **P**. Constitutive relations for **D**, **B** and $\mathbf{J}_\mathrm{f}$ read:

$$\mathbf{D} = \epsilon_0 \epsilon \mathbf{E}, \tag{1.7}$$

$$\mathbf{B} = \mu_0 \mu \mathbf{H}, \tag{1.8}$$

$$\mathbf{J}_\mathrm{f} = \sigma \mathbf{E}, \tag{1.9}$$

where $\sigma$ is the conductivity and $\mu = 1$ is the relative permeability of the nonmagnetic medium. Inserting 1.7 into 1.5 we get a relation for the polarization:

$$\mathbf{P} = \epsilon_0(\epsilon - 1)\mathbf{E}, \tag{1.10}$$

term $(\epsilon - 1)$ expresses how the material is polarized in the presence of electric field and is often called the dielectric susceptibility $\chi$ and $\epsilon$ is called the dielectric constant. For majority of materials $\epsilon$ is not constant and is frequency dependent. In such case it is usually called the dielectric function.

## 1.2 Dielectric function of matter

Propagation of the electromagnetic waves in matter can be described using the dielectric function $\epsilon$. Optical response of materials depends on the frequency $\omega$ and possibly on the wave vector **K**. For such dependence non-locality in time and space must be taken into account and Equations 1.7 and 1.9 must be rewritten:

$$\mathbf{D}(\mathbf{r},t) = \epsilon_0 \int dt' \mathbf{dr}' \epsilon(\mathbf{r} - \mathbf{r}', t - t') \mathbf{E}(\mathbf{r}', t'), \tag{1.11}$$

$$\mathbf{J}(\mathbf{r},t) = \int dt' \mathbf{dr}' \sigma(\mathbf{r} - \mathbf{r}', t - t') \mathbf{E}(\mathbf{r}', t'). \tag{1.12}$$

Here we assume that all length scales are significantly larger than the lattice constant of the material, ensuring homogeneity [10, p. 8]. Impulse response functions depend only on differences of temporal and spatial coordinates. Equations 1.11 and 1.12 can be simplified by applying the Fourier transform which turns the convolution into the multiplication. An original field is decomposed into plane wave components with given

$\mathbf{K}$ and $\omega$:

$$\mathbf{D}(\mathbf{K},\omega) = \epsilon_0\epsilon(\mathbf{K},\omega)\mathbf{E}(\mathbf{K},\omega), \tag{1.13}$$

$$\mathbf{J}(\mathbf{K},\omega) = \sigma(\mathbf{K},\omega)\mathbf{E}(\mathbf{K},\omega). \tag{1.14}$$

Taking these two equations, Equation 1.5 and $\mathbf{J} = \frac{\partial \mathbf{P}}{\partial t}$ we can arrive to the equation linking the dielectric function and the conductivity together.

$$\epsilon(\mathbf{K},\omega) = 1 + \frac{\mathrm{i}\sigma(\mathbf{K},\omega)}{\epsilon_0\omega}. \tag{1.15}$$

This relation claims that we can describe the optical properties of material either by its conductivity or the dielectric function. The real part of $\epsilon$ describes polarization and the imaginary part stands for absorption. In contrast, the real part of $\sigma$ describes conductivity and imaginary part depicts polarization of the system when the driving field is present. As long as the lattice constant and the mean free path of electrons in the material are significantly shorter than the wavelength of the electromagnetic wave in it, the wave vector dependence does not need to be considered and following simplification $\epsilon(\mathbf{K} = \mathbf{0}, \omega) = \epsilon(\omega)$ is valid. For metals, this assumption is well accurate till we get to ultraviolet frequencies. The dielectric function can be generally complex valued, $\epsilon(\omega) = \epsilon_1(\omega) + \mathrm{i}\epsilon_2(\omega)$. One may alternatively use the complex refractive index $N(\omega) = n(\omega) + \mathrm{i}\kappa(\omega)$. $N$ and $\epsilon$ describe the same properties of matter but in different area of physics one of them is usually preferred. The following relations are linking these two quantities together:

$$N = \sqrt{\epsilon}, \tag{1.16}$$

$$\epsilon_1 = n^2 - \kappa^2, \tag{1.17}$$

$$\epsilon_2 = 2n\kappa, \tag{1.18}$$

$$n = \sqrt{\frac{\epsilon_1 + \sqrt{\epsilon_1^2 + \epsilon_2^2}}{2}}, \tag{1.19}$$

$$\kappa = \frac{\epsilon_2}{2n}, \tag{1.20}$$

where $\kappa$ is the extinction coefficient which is linked with the absorption coefficient $\alpha$ by the relation:

$$\alpha(\omega) = \frac{2\omega\kappa(\omega)}{c}. \tag{1.21}$$

Both coefficients describe optical absorption of an electromagnetic wave propagating through the material. Exponential attenuation of a beam with intensity $I_0$ when propagating through the material of thickness $l$ is given by the Beer's law [13, s. 219]:

$$I(l) = I_0 e^{-\alpha l}, \tag{1.22}$$

we automatically assumed that the absorption coefficient does not vary with spatial coordinates but only with frequency and type of material.

Absorption and material losses depend on the imaginary part of the dielectric function. Although both $\epsilon_1$ and $\epsilon_2$ can be experimentally determined using ellipsometry for example, there exist theoretical models such as Cauchy, Lorentz, Drude and Sellmeier model. These models were derived at the beginning of the 20th century when the accuracy of contemporary experimental techniques was much worse than nowadays. Analytical models are still in use mainly due to their simplicity and good agreement. They also link measured values with system properties such as interband transitions, dispersion branches etc. Next, we will mention the Drude model which we use for modelling the dielectric function of metals.

## 1.3 Drude model

In metals, some valence electrons are no longer bound to the atom cores and form so-called electron gas. These electrons interact with the atom cores in a very different way. The atom cores form an effective potential in crystal thus electrons are affected by interaction with all cores rather than by interaction with the atom they originate from. Consequently, the electrons can react to an external field and move inside the metal almost freely. Their motion is damped via the mutual collisions with the frequency $\gamma$ which is the inverse value of the relaxation time $\tau$. Such electrons could be described as a system of independent, identical, isotropic harmonic oscillators of mass $m$ with no restoring force present ($k\mathbf{x} = 0$). The equation of motion is following:

$$m\ddot{\mathbf{x}} + m\gamma\dot{\mathbf{x}} = -e\mathbf{E}. \tag{1.23}$$

Assuming that the external electric field is harmonic time dependent $\mathbf{E}(t) = \mathbf{E}_0\exp(-\mathrm{i}\omega t)$ the displacement of electron is:

$$\mathbf{x}(t) = \frac{e/m}{\omega^2 + \mathrm{i}\gamma\omega}\mathbf{E}(t). \tag{1.24}$$

The external field moves all the electrons with respect to the atom cores and metal is polarized. For dielectric function of metal we then get:

$$\epsilon(\omega) = \epsilon_\infty - \frac{\omega_\mathrm{p}^2}{\omega^2 + \mathrm{i}\gamma\omega}, \tag{1.25}$$

where $\omega_\mathrm{p}^2 = ne^2/\epsilon_0 m$ is the plasma frequency of the free electron gas and $\epsilon_\infty$ is high-frequency permittivity of the metal. Previous equation is complex. We can split it to real part $\epsilon_1$

$$\epsilon_1(\omega) = \epsilon_\infty - \frac{\omega_\mathrm{p}^2\tau^2}{1 + \omega^2\tau^2}, \tag{1.26}$$

and imaginary part $\epsilon_2$

$$\epsilon_2(\omega) = \frac{\omega_\mathrm{p}^2\tau}{\omega(1 + \omega^2\tau^2)}, \tag{1.27}$$

where we have used $\gamma = \frac{1}{\tau}$. For frequencies close to the $\omega_{\mathrm{p}}$, the collision frequency $\gamma \ll \omega$ and the damping is negligible. If we put $\gamma = 0$ into 1.25, we get following approximative relation:

$$\epsilon(\omega) = \epsilon_{\infty} - \frac{\omega_{\mathrm{p}}^2}{\omega^2}. \tag{1.28}$$

# 2. Plasmons

In the previous chapter, we described the properties of electromagnetic waves in a homogeneous material. Another step crucial for understanding how plasmonic antennas work is to explain the origin of surface plasmon polariton (SPP) and localized surface plasmon (LSP). These quasiparticles combine oscillations of conductive electrons and electromagnetic surface wave. They propagate along the dielectric-conductor interface and are evanescently confined in the perpendicular direction. Next, we will describe the dispersion relation and spatial profile of mentioned waves. However, at first, we will derive the wave equation.

## 2.1 The wave equation at interface

If we apply the curl ($\nabla\times$) to the Maxwell equation 1.3 we get:

$$\nabla \times \nabla \times \mathbf{E} = -\frac{\partial(\nabla \times \mathbf{B})}{\partial t}, \tag{2.1}$$

in this case, we can limit ourselves to space without free charges and free currents ($\rho_\mathrm{f} = 0$ and $\mathbf{J}_\mathrm{f} = 0$). We can combine Equations 1.4, 1.6 and 2.1 and we can get:

$$\nabla \times \nabla \times \mathbf{E} = -\mu_0 \frac{\partial^2 \mathbf{D}}{\partial t^2}. \tag{2.2}$$

In the next step, we will apply the vector identity $\nabla \times \nabla \times \mathbf{E} \equiv \nabla(\nabla \cdot \mathbf{E}) - \nabla^2\mathbf{E}$ and a product rule $\nabla \cdot (\epsilon\mathbf{E}) \equiv \mathbf{E} \cdot \nabla\epsilon + \epsilon\nabla \cdot \mathbf{E}$. When also $\mathbf{D}$ is replaced using Equation 1.7, Equation 2.1 changes to:

$$\nabla(-\frac{1}{\epsilon}\mathbf{E} \cdot \nabla\epsilon) - \nabla^2\mathbf{E} = -\mu_0\epsilon_0\epsilon\frac{\partial^2 \mathbf{E}}{\partial t^2}. \tag{2.3}$$

Assuming negligible spatial variation of the dielectric function ($\nabla\epsilon = 0$), previous equation simplifies to the central equation of electromagnetic wave theory called the wave equation:

$$\nabla^2\mathbf{E} - \frac{\epsilon}{c^2}\frac{\partial^2 \mathbf{E}}{\partial t^2} = 0. \tag{2.4}$$

For harmonic time dependent electric field $\mathbf{E}(\mathbf{r},t) = \mathbf{E}(\mathbf{r})\exp(-\mathrm{i}\omega t)$, Equation 2.4 transforms to so-called Helmholtz equation:

$$\nabla^2\mathbf{E} + k_0^2\epsilon\mathbf{E} = 0, \tag{2.5}$$

where $k_0 = \frac{\omega}{c}$ is the wave vector of the propagating wave. Note, that equation 2.5 is not time dependent and may be solved separately in regions of constant $\epsilon$.

## 2.2 Surface plasmon polaritons

The simplest geometry with regions of various $\epsilon$ consists of only a single interface dividing free space into two parts. An example of such geometry is shown in Figure 2.1. Here $\epsilon = \epsilon(z)$ and for $z > 0$ the half-space is described by positive real dielectric function $\epsilon_2$ representing non-absorbing medium and for $z < 0$ we have an absorbing material with dielectric function $\epsilon_1(\omega)$. Let's assume that our absorbing material has a metallic character which implies $\mathrm{Re}\{\epsilon_1\} < 0$. In the $xy$ plane the interface is infinite. At such interface ($z = 0$) excitation of SPP is possible. We will assume that the surface

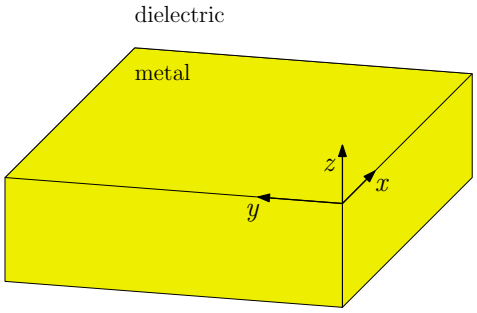


Figure 2.1: Single interface geometry dividing free space into dielectric and metallic half spaces. Interface is infinite in the $xy$ plane.

wave propagates along the $x$ axis. SPP is described as the wave $\mathbf{E}(x,z) = \mathbf{E}(z)\exp(\mathrm{i}\beta x)$. The propagation constant $\beta$ is a complex parameter and corresponds to the component of the wave vector in the direction of propagation $\beta = k_x$. Inserting the expression for SPP into the Helmholtz equation 2.5 yields:

$$\frac{\partial^2\mathbf{E}(z)}{\partial z^2} + (k_0^2\epsilon - \beta^2)\mathbf{E} = 0. \tag{2.6}$$

A similar equation holds for the magnetic field $\mathbf{H}$. These equations have six components altogether and we will use Equations 1.3 and 1.4 to find an explicit solution for all of them. We have already assumed harmonic time dependence of wave ($\frac{\partial}{\partial t} \to -\mathrm{i}\omega$). Set of coupled equations is:

$$\frac{\partial E_z}{\partial y} - \frac{\partial E_y}{\partial z} = \mathrm{i}\omega\mu_0 H_x, \tag{2.7}$$

$$\frac{\partial E_x}{\partial z} - \frac{\partial E_z}{\partial x} = \mathrm{i}\omega\mu_0 H_y, \tag{2.8}$$

$$\frac{\partial E_y}{\partial x} - \frac{\partial E_x}{\partial y} = \mathrm{i}\omega\mu_0 H_z, \tag{2.9}$$

$$\frac{\partial H_z}{\partial y} - \frac{\partial H_y}{\partial z} = -\mathrm{i}\omega\epsilon_0\epsilon E_x, \tag{2.10}$$

$$\frac{\partial H_x}{\partial z} - \frac{\partial H_z}{\partial x} = -\mathrm{i}\omega\epsilon_0\epsilon E_y, \tag{2.11}$$

$$\frac{\partial H_y}{\partial x} - \frac{\partial H_x}{\partial y} = -\mathrm{i}\omega\epsilon_0\epsilon E_z. \tag{2.12}$$

We have chosen the wave to propagate in the $x$-direction which implies $\frac{\partial}{\partial x} = \mathrm{i}\beta$ and $\frac{\partial}{\partial y} = 0$. This system of equations allows two solutions having different polarization. First solution corresponds to the transverse magnetic (TM) mode, where only $E_x$, $E_z$ and $H_y$ are nonzero components. Second solution corresponds to the transverse electric (TE) mode with nonzero $E_y$, $H_x$ and $H_z$. TM mode is described by following equations:

$$E_x = -\mathrm{i}\frac{1}{\omega\epsilon_0\epsilon}\frac{\partial H_y}{\partial z}, \tag{2.13}$$

$$E_z = -\frac{\beta}{\omega\epsilon_0\epsilon}H_y, \tag{2.14}$$

$$\frac{\partial^2 H_y}{\partial z^2} + (k_0^2\epsilon - \beta^2)H_y = 0, \tag{2.15}$$

and TE mode by corresponding equations:

$$H_x = -\mathrm{i}\frac{1}{\omega\mu_0}\frac{\partial E_y}{\partial z}, \tag{2.16}$$

$$H_z = -\frac{\beta}{\omega\mu_0}E_y, \tag{2.17}$$

$$\frac{\partial^2 E_y}{\partial z^2} + (k_0^2\epsilon - \beta^2)E_y = 0. \tag{2.18}$$

However, further analysis of TE mode equations shows that TE mode is not a solution of Maxwell equations and no surface modes exist for TE polarization [10, p. 27]

Now we will return to our geometry shown in Figure 2.1. First we will look at the solutions of TM modes given by Equations 2.13–2.15. For half space $z > 0$ it yields:

$$H_y(z) = A_2 e^{\mathrm{i}\beta x} e^{-k_2 z}, \tag{2.19}$$

$$E_x(z) = \mathrm{i}A_2\frac{1}{\omega\epsilon_0\epsilon_2}k_2 e^{\mathrm{i}\beta x} e^{-k_2 z}, \tag{2.20}$$

$$E_z(z) = -A_2\frac{\beta}{\omega\epsilon_0\epsilon_2}e^{\mathrm{i}\beta x} e^{-k_2 z}, \tag{2.21}$$

and for $z < 0$:

$$H_y(z) = A_1 e^{\mathrm{i}\beta x} e^{k_1 z}, \tag{2.22}$$

$$E_x(z) = -\mathrm{i}A_1\frac{1}{\omega\epsilon_0\epsilon_1}k_1 e^{i\beta x} e^{k_1 z}, \tag{2.23}$$

$$E_z(z) = -A_1 \frac{\beta}{\omega \epsilon_0 \epsilon_1} e^{\mathrm{i}\beta x} e^{k_1 z}, \tag{2.24}$$

where $k_1$ and $k_2$ represents the component of the wave vector perpendicular to the interface in metal and dielectric, respectively. Using boundary continuity condition of $H_y$ and $\epsilon_i E_z$ at the interface requires that $A_1 = A_2$ and $H_y$ has to fulfil similar wave equation as 2.6:

$$\frac{k_2}{k_1} = -\frac{\epsilon_2}{\epsilon_1}, \tag{2.25}$$

$$k_1^2 = \beta^2 - k_0^2 \epsilon_1, \tag{2.26}$$

$$k_2^2 = \beta^2 - k_0^2 \epsilon_2. \tag{2.27}$$

Note that these waves exist only at interfaces between materials with different signs of the real part of the dielectric function, e.g. between conductor and dielectric media. Combining these three equations we get the dispersion relation of SPP:

$$\beta = k_0 \sqrt{\frac{\epsilon_1 \epsilon_2}{\epsilon_1 + \epsilon_2}}. \tag{2.28}$$

## 2.3 Localized surface plasmons

Metal and dielectric media in the previous section were not confined in space and formed infinitely extended interface. Such geometry gives arise to SPP. The second fundamental excitation of plasmonics is supported by metal structures of finite dimensions. Spatial confinement leads to the formation of the standing wave pattern where only the waves satisfying boundary conditions can exist. This leads to resonant-like properties of plasmonic antennas.

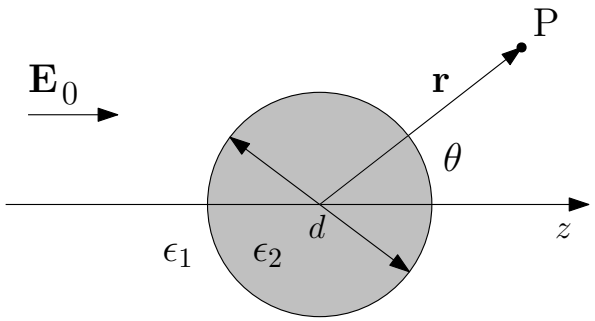


Figure 2.2: Homogeneous, isotropic, spherical particle in constant electric field. Taken from [10, p. 66].

To describe an interaction of the electromagnetic wave with nanoparticle we will use an example of a homogeneous, isotropic, spherical particle. The diameter of the particle is $d$, the dielectric constant is $\epsilon_2$ and the sphere is embedded in non-absorbing and isotropic dielectric medium described by $\epsilon_1$ (Figure 2.2). We will consider that the sphere diameter $d$ is much smaller than the wavelength of electromagnetic radiation $\lambda$. This condition is normally fulfilled for plasmonic resonators and allows us to use so-called *quasistatic approximation*. Since $d \ll \lambda$, the phase of the electromagnetic

wave is considered to be constant for the entire sphere. Therefore, the electric field driving the particle can be approximated as static, $\mathbf{E} = E_0\mathbf{z}$. A solution of stationary problem is given by Laplace equation $\nabla^2\phi = 0$, where $\phi$ is electric potential and $\mathbf{E} = -\nabla\phi$. A solution of the Laplace equation is series of Legendre polynomials [10, p. 67]. In order to get the field intensity $\mathbf{E}_{\text{in}}$ inside and $\mathbf{E}_{\text{out}}$ outside at point of interest $P$, application of boundary conditions and defining dipole moment $\mathbf{p}$ as:

$$\mathbf{p} = 4\pi\epsilon_0\epsilon_1 \left(\frac{d}{2}\right)^3 \frac{\epsilon_2 - \epsilon_1}{\epsilon_2 + 2\epsilon_1}\mathbf{E}_0. \tag{2.29}$$

is necessary. Following [10, p. 67] the electric field reads:

$$\mathbf{E}_{\text{in}} = \frac{3\epsilon_1}{\epsilon_2 + 2\epsilon_1}\mathbf{E}_0, \tag{2.30}$$

$$\mathbf{E}_{\text{out}} = \frac{3\mathbf{n}\left(\mathbf{n}\cdot\mathbf{p}\right) - \mathbf{p}}{4\pi\epsilon_0\epsilon_1} \cdot \frac{1}{r^3}, \tag{2.31}$$

where $\mathbf{n}$ is the unit vector pointing towards the point of interest.

We see that the electric field induce the dipole moment inside the spherical particle. The proportionality coefficient between the field we have applied and induced dipole moment is the polarizability $\alpha$ defined as:

$$\mathbf{p} = \epsilon_0\epsilon_1\alpha\mathbf{E}_0. \tag{2.32}$$

From Equation 2.29 $\alpha$ is:

$$\alpha = 4\pi \left(\frac{d}{2}\right)^3 \frac{\epsilon_2 - \epsilon_1}{\epsilon_2 + 2\epsilon_1}. \tag{2.33}$$

This term is maximal for frequencies where minimal value of the $|\epsilon_2 + 2\epsilon_1|$ is reached. It corresponds to resonant enhancement of the polarizability. This enhancement is limited since $\text{Im}[\epsilon_2 \neq 0]$.

At this point, we will leave the static case and use the quasistatic approach where the ideal dipole approximation is still valid instead. This will allow us to think about time-varying fields but neglect spatial retardation at the same time. In the resonance, both internal and dipolar fields are enhanced and the sphere acts as an oscillating electric dipole. The total electric field $\mathbf{E}$ and magnetic field $\mathbf{H}$ in general form are [14, p. 411]:

$$\mathbf{E} = \frac{1}{4\pi\epsilon_0}\left\{k^2\left(\mathbf{n}\times\mathbf{p}\right)\times\mathbf{n}\frac{e^{\mathrm{i}kr}}{r} + \left[3\mathbf{n}\left(\mathbf{n}\cdot\mathbf{p}\right) - \mathbf{p}\right]\left(\frac{1}{r^3} - \frac{\mathrm{i}k}{r^2}\right)e^{\mathrm{i}kr}\right\}, \tag{2.34}$$

$$\mathbf{H} = \frac{ck^2}{4\pi}\left(\mathbf{n}\times\mathbf{p}\right)\frac{e^{\mathrm{i}kr}}{r}\left(1 - \frac{1}{\mathrm{i}kr}\right). \tag{2.35}$$

These terms are a bit complicated, thus we will focus on a special case where $d \ll r \ll \lambda$. Therefore, we examine fields very near to our dipole source (the static zone). Equa-

tion 2.34 turns into Equation 2.31 and for $\mathbf{H}$ we get:

$$\mathbf{H} = \frac{\mathrm{i}ck}{4\pi} (\mathbf{n} \times \mathbf{p}) \frac{1}{r^2}. \tag{2.36}$$

Note that the magnetic field magnitude is much smaller than the electric one. For static field, the magnetic field vanishes completely since it is induced by current flowing through the structure.

Resonantly enhanced polarizability also affects scattering and absorption of resonator. The cross section $C_{\mathrm{sca}}$ and $C_{\mathrm{abs}}$ for scattering and absorption, respectively are:

$$C_{\mathrm{sca}} = \frac{k^4}{6\pi} |\alpha|^2 = \frac{8\pi}{3} k^4 \left(\frac{d}{2}\right)^6 \left|\frac{\epsilon_2 - \epsilon_1}{\epsilon_2 + 2\epsilon_1}\right|^2, \tag{2.37}$$

$$C_{\mathrm{abs}} = k\mathrm{Im}\left[\alpha\right] = 4\pi k \left(\frac{d}{2}\right)^3 \mathrm{Im}\left[\frac{\epsilon_2 - \epsilon_1}{\epsilon_2 + 2\epsilon_1}\right]. \tag{2.38}$$

# 3. Electron paramagnetic resonance

Although this thesis mainly focuses on the design and optimization of plasmonic antennas for high wavelengths it also seeks some applications. In the next chapters, we will show that plasmonic antennas are able to focus electromagnetic radiation to very small volumes and produce strongly enhanced electric and magnetic fields in their vicinity. One may use such enhancement in spectroscopic techniques as electron paramagnetic resonance (EPR) for enhancing a signal or lowering the detection limit. In this chapter, the fundamentals of electron paramagnetic resonance will be discussed following the book [15].

## 3.1 Introduction to EPR

Knowledge of the molecule structure and energy level diagram is crucial for the prediction of material properties. Most of this knowledge is based on the analysis of molecular absorption spectra. Usually we measure how a beam of electromagnetic radiation passes through a sample of our interest. Every line or band in the spectrum represents a radiative transition between (two) energy states. Some molecules contain a magnetic dipole that can interact with electromagnetic radiation. One of the methods dealing with this type of interaction is EPR. In principle, the EPR is very similar to the common commercially used and better known nuclear magnetic resonance (NMR) technique. However, in EPR magnetic moments arise from electrons rather than nuclei.

Quantum mechanics postulates that every elementary particle has an angular momentum called the spin $\mathbf{S}$. The spin results in the electron magnetic dipole moment $\boldsymbol{\mu}_\mathrm{S}$ given by:

$$\boldsymbol{\mu}_\mathrm{S} = -\frac{g_\mathrm{e} e}{2m_\mathrm{e}}\mathbf{S}, \tag{3.1}$$

where $m_\mathrm{e} = 9.109 \cdot 10^{-31}\,\mathrm{kg}$ is the electron mass, $e = -1.602 \cdot 10^{-19}\,\mathrm{C}$ is the electron charge and $g_\mathrm{e}$ is the effective Zeeman factor. The spin is referred to as moving along its own particle axis. Even though this idea is not correct, it is at least illustrative. The angular momentum takes only specific values:

$$S^2 = s\,(s+1)\,\hbar^2, \tag{3.2}$$

where $\hbar$ is Planck constant $h$ divided by $2\pi$ and $s$ is the spin quantum number. Projection of $\mathbf{S}$ to the $z$ direction is also quantized using the spin magnetic quantum

number $m_\mathrm{s}$:

$$S_z = m_\mathrm{s}\hbar. \tag{3.3}$$

If we now limit ourselves to free electron, then $m_\mathrm{s} = \pm\frac{1}{2}$ and the component $\mu_z$ of the electron spin magnetic moment $\mu$ along the $z$ direction is:

$$\mu_z = -g_\mathrm{e}\mu_\mathrm{B}M_\mathrm{S}, \tag{3.4}$$

where $\mu_\mathrm{B} = -\frac{\hbar e}{2m_\mathrm{e}} = 9.27 \cdot 10^{-24}\,\mathrm{JT}^{-1}$. Minus sign arises because electron charge is negative by definition. Energy of $\mu_z$ in external magnetic field $\mathbf{B}_0$ is given by dot product:

$$E = -\boldsymbol{\mu}_z \cdot \mathbf{B}_0, \tag{3.5}$$

If the magnetic moment orientation is parallel to the static magnetic field $\mathbf{B}_0$ the energy is:

$$E = -\mu_z B_0. \tag{3.6}$$

## 3.2 Zeeman effect

In the presence of an external, static magnetic field single spectral line may split into several separated lines. The energy of transition represents a given atomic state; therefore, spectral line splitting is a consequence of atomic sub-states presence. This phenomenon is named after Dutch physicist Pieter Zeeman.

For simplicity let us again assume a system consisting of only one electron. This electron is unpaired and has two possibilities of spin orientation. In zero magnetic field, the energy levels for both spin orientation are the same. If we now put our electron into a non-zero magnetic field $\mathbf{B}_0$, the energy levels will split into two. The energy of these states is given by:

$$E = g_e\mu_B B_0 m_s, \tag{3.7}$$

A single electron may have the spin quantum number $m_s = +\frac{1}{2}$ or $m_s = -\frac{1}{2}$ and the corresponding energy difference $\Delta E$ between these states is:

$$\Delta E = g_e\mu_B B_0. \tag{3.8}$$

The energy level diagram of the single electron is shown in Figure 3.1. To change its spin orientation via radiative transition, the electron needs to absorb or emit a photon. For absorption to occur we need a photon which energy equals the energy difference between electron states. The energy of photon is:

$$E = h\nu, \tag{3.9}$$

where $\nu$ is the frequency of the photon. Putting Equation 3.9 into 3.8 we get the photon absorption condition:

$$h\nu = g_e\mu_B B_0. \tag{3.10}$$

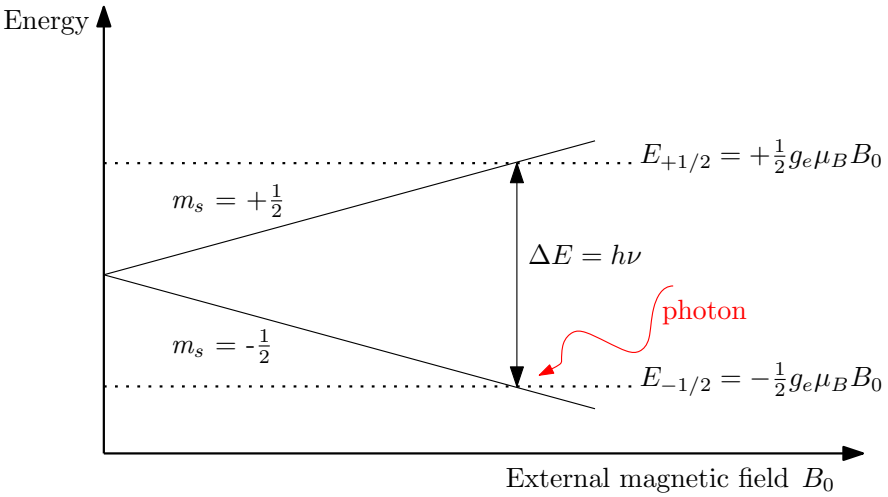


Figure 3.1: Schematic energy-level diagram of free electron. It shows energy level splitting in nonzero external magnetic field.

Another condition necessary for the absorption process is that magnetic field component B of incoming radiation must be able to interact with the electron magnetic dipoles and populates them up. Fulfilling this condition is possible unless the magnetic field component **B** is parallel or antiparallel to the electron magnetic dipole moment.

## 3.3 HFEPR setup in Stuttgart

Institute of Physical Chemistry at the University of Stuttgart provides measurements of high-frequency electron paramagnetic resonance (HFEPR) with an in-house developed spectrometer. HFEPR is one of the most promising electron spin resonance techniques since it is capable of measuring 3D samples without their elaborate preparation. It also has good spin sensitivity [16]. The instrument in Stuttgart operates in the frequency range from 80 GHz to 1100 GHz. A superconducting solenoid magnet can induce field up to 17 T for temperatures below 4.2 K. In the following section, we will describe the generation, propagation and detection of microwaves in the HFEPR setup.

The microwave source is controlled by a computer synthesizer which provides output ranging from 8 GHz to 20 GHz. Radiation is then modified by an amplifier-multiplier chain to the base frequency range 80–125 GHz. To obtain higher frequencies, a combination of full-band frequency multipliers is employed. However, this multiplication process leads to significant decrease in output power. The source power is reduced ca. by the factor of 2 (−3 dB) for every following higher frequency range. Figure 3.2 shows the output power of the source in more detail. The maximum power of the source power is 37 mW near 100 GHz and drops to about 0.01 mW for frequency band 800–1100 GHz.

The optical path of radiation emitted by the microwave source could be divided into two parts. Outside a cryostat of the magnet, radiation propagates in a form of a Gaussian beam and is coupled into quasi-optics using a corrugated horn. This element guides the radiation more preferably in a forward direction. Then there are

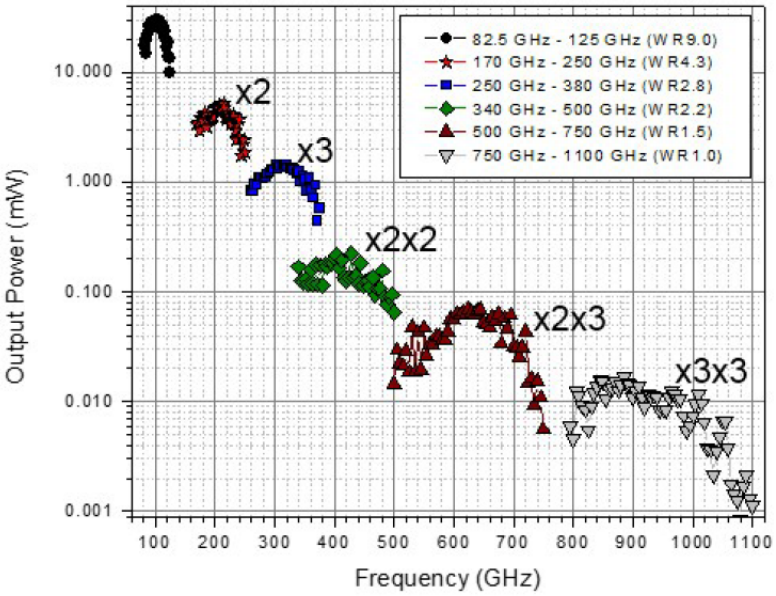


Figure 3.2: Frequency dependence of the power output. It shows significant decrease of radiated power. Maximum power is 37 mW, whereas the lowest drops to about 0.01 mW. Numbers next to the power curves indicate level of frequency multiplication. Taken from [8], supplementary files.

optical elements such as an off-axial mirror (it ensures the beam refocuses after the distance of 250 mm), a vertical wire grid polarizer (it defines polarization of the beam), a Faraday rotator, etc. Later the radiation is coupled into a corrugated waveguide which guides the beam inside the cryostat. At the sample position, the waveguide is tapered in order to focus the beam onto the sample with dimensions up to a few millimetres. In so-called induction mode [17] the radiation passes through the sample, it is reflected from the gold mirror at the bottom of the substrate (onto which the sample is placed), passes through the sample for the second time, and propagates towards the detector. Multiple reflections of the radiation inside the substrate may occur aswell. Part of the radiation carrying the EPR signal has different polarization than the original microwave and is easily isolated by another polarizer. The EPR signal is then detected by liquid helium cooled bolometer or zero bias detector.

To sum up, one way leading to the enhancement of sample EPR signal is to enhance the power of the source. However, the power is strongly decreasing for higher frequency bands. This negatively affects all the measurements since it decreases the signal to noise ratio. Another way to enhance the EPR signal could be based on the resonant enhancement of the high-frequency magnetic field in the sample vicinity. We have already described resonant properties of LSP in Section 2.3. Plasmonic antennas are devices based on this phenomenon. They are frequently used for their ability to enhance electric and magnetic field [18], [19], [20].

# 4. Effective layer model

This chapter introduces a semi-analytical model that allows to examine magnetic field enhancement provided by dielectric substrate with a metallic mirror at the bottom and optionally also with plasmonic antennas at the top. Physical presence of the mirror in a simulation area frequently leads to a significant increase in computational complexity. Presented model aims to determine resonant properties and magnetic field enhancement without the need for numerical simulations of the mirror. The method is based on a combination of analytically calculated Fresnel coefficients of interfaces and numerically obtained scattered field of a single antenna. The mirror is taken into account effectively; therefore, this model is referred to as the effective layer model (ELM).

Let us start our description by defining the geometry of our problem (Figure 4.1). The dielectric substrate of thickness $d$ has the metallic mirror at the bottom. The mirror is considered to be thick enough to reflect all the radiation. This is well fulfilled for thickness larger than the skin depth of radiation. Above the substrate, there is another dielectric material, e.g. air. Materials are represented by their index of refraction.

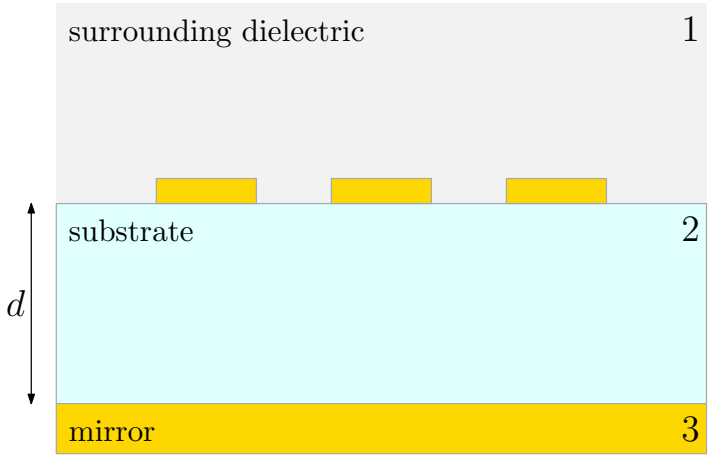


Figure 4.1: ELM geometry scheme.

The enhancement of the EPR signal is based on the ability to enhance the magnetic field near an absorbing material, that needs to be positioned in the vicinity of the plasmonic antenna. The magnetic field near the antenna is induced by current oscillating in the antenna. How the current flows can be described by the current distribution $\mathbf{P}(\mathbf{r},\omega)$. Therefore, there is a relation of proportionality between the magnetic field

and the current distribution.

$$\mathbf{H}(\mathbf{r},\omega) \propto \mathbf{P}(\mathbf{r},\omega). \tag{4.1}$$

Here we assume that the antenna response is governed by a single mode and the overall current distribution can be expressed as the current distribution $\mathcal{P}(\mathbf{r},\omega)$ of this particular mode times its excitation amplitude $p(\omega)$. This assumption is well satisfied in the THz frequency region, where distinct modes are spectrally well separated.

$$\mathbf{P}(\mathbf{r},\omega) = p(\omega)\mathcal{P}(\mathbf{r},\omega). \tag{4.2}$$

Mode spatial distribution is given by the antenna geometry. The excitation amplitude is proportional to the total electric field driving the antenna. This field can be broken down into two contributions: $E_0$ represents the original field emitted by the source (approximated by plane wave or Gaussian beam) and $E_{\mathrm{sca}}$, which represents the field emitted/scattered by the system of the antenna and the mirror. Therefore, $p(\omega)$ is:

$$p(\omega) = \alpha(\omega)\left[E_0(\omega) + E_{\mathrm{sca}}(\omega)\right], \tag{4.3}$$

where $\alpha$ is the polarizability factor. This equation is analogous to Equation 2.32. The fact that the antenna affects itself at later times, i.e. is driven by its own scattered field can be mathematically put as:

$$p(\omega) = \alpha(\omega)\left[E_0(\omega) + g(\omega)p(\omega)\right], \tag{4.4}$$

where $g(\omega)$ is the antenna feedback factor. We can rewrite previous equation for excitation amplitude into the form:

$$p(\omega) = \frac{\alpha(\omega)E_0}{1 - \alpha(\omega)g(\omega)}. \tag{4.5}$$

Large field enhancement could be reached when the denominator of Equation 4.5 is close to zero, i.e. for values $\alpha(\omega)\cdot g(\omega)$ close to 1. The field enhancement factor could be defined as the ratio between original excitation amplitude $p_0(\omega)$ evaluated in the absence of the mirror and excitation amplitude $p(\omega)$. This ratio is [Martin Hrtoň, private communication]:

$$\frac{p(\omega)}{p_0(\omega)} = \frac{\dfrac{1 + \frac{r_{12}+r_{23}e^{2ik_2d}}{1-r_{21}r_{23}e^{2ik_2d}}}{1 + r_{12}}}{1 + \dfrac{E^{\downarrow}}{1 - r_{12}}\dfrac{t_{21}r_{23}e^{2ik_2d}}{1 + r_{21}r_{23}e^{2ik_2d}}}, \tag{4.6}$$

where $k_2$ is the wave vector in the substrate, $E^{\downarrow}$ is the normalized downward emitted wave, $r_{ij}$ and $t_{ij}$ are Fresnel amplitude reflection and transmission coefficients, respectively. The downward emitted wave is given by the polarizability and antenna feedback factor. $E^{\downarrow}$ also represents the resonant properties of the antennas and their contribution to the overall enhancement. In $s$-polarization notation the Fresnel coefficients can

be written as:

$$r_{ij} = \frac{n_i - n_j}{n_i + n_j}, \qquad t_{ij} = \frac{2n_i}{n_i + n_j}. \tag{4.7}$$

Note, that these coefficients do not consider the presence of the gold antennas at the top surface of the substrate. Since we use a perpendicular irradiation, the notation of Fresnel coefficients does not affect the field enhancement factor.

Finally, the overall enhancement in the ELM model is the product of the field enhancement factor and normalized second power of mean magnetic field **H** induced by the antennas. These values might be, at least qualitatively, compared with the normalized second power of mean magnetic field **H** obtained by other simulation containing the gold mirror. Proportional relation between the field enhancement factor and field values from the other simulation yields:

$$\frac{|\mathbf{H^2}|}{|H_0^2|} \propto \left| \frac{p(\omega)}{p_0(\omega)} \right|^2 . \tag{4.8}$$

Here $H_0$ represents value of the magnetic field obtained in the simulation without the antennas and the gold mirror. It represents normalization value.

So far, we have demonstrated the analytical part of the ELM. In Section 6.1 we will show how to obtain the values of source and scattered field using computational software. Before we do so, we will turn our attention to basic simulation methods and their principles.

# 5. Simulation methods

In recent decades as the computational power of computers has increased and its cost decreased by few orders of magnitudes, a new approach (*in silico*) of studying plasmonic resonators based on numerical simulations of their properties was developed. Until then known analytical methods, such as Mie theory, were applicable only to planar geometries or to very few simple shapes such as cylinders, spheres and so on. In contrast with that, numerical methods allow to solve almost any geometry.

In this chapter, the overview of numerical solution techniques will be presented at first. Then the principles of Finite-Difference in Time-Domain (FDTD) will be demonstrated. FDTD method is currently used by many scientific groups all over the world.

**Green Dyadic Method (GDM)**[21]
GDM deals with structures of finite volume $V$ embedded in two semi-infinite dielectric media. System is irradiated by a plane, harmonic, time-dependent wave in a form of $\exp(-\mathrm{i}\omega t + \mathrm{i}\mathbf{k}\cdot\mathbf{r})$. The electric field of such wave satisfies the wave equation 2.4. Solution of this equation is the sum of the incident field $\mathbf{E}_0$ and field scattered by the resonator denoted as $\mathbf{E}_\mathrm{S}$:

$$\mathbf{E}(\mathbf{r},\omega) = \mathbf{E}_0(\mathbf{r},\omega) + \mathbf{E}_\mathrm{S}(\mathbf{r},\omega). \tag{5.1}$$

If we want to calculate the field scattered by the resonator we need to find out the electric field inside the resonator and response of the reference system to a point source (Green's function) at first. We achieve this by discretization of resonator volume into $N$ finite-size cells and calculating the electric field in each of them. It leads to the system of $N$ linear equations which are numerically solved.

$$\mathbf{E}(\mathbf{r},\omega) = \mathbf{E}_0(\mathbf{r},\omega) + V\sum_{1}^{N} \overleftrightarrow{G}_{\mathrm{ref}}(\mathbf{r},\mathbf{r}_i)\mathbf{E}(\mathbf{r}_i,\omega), \tag{5.2}$$

where $V$ is the volume of one cell and $\overleftrightarrow{G}_{\mathrm{ref}}$ describes the electric field emitted at $\mathbf{r}'$ and observed at r. $\overleftrightarrow{G}_{\mathrm{ref}}$ is the dyadic Green's function.

GDM is a frequency-domain technique that can easily treat arbitrary material dispersion. Since it is based on the discretization of metallic resonator volume, very fine nonuniform or nonorthogonal grids are required for complex geometry structures. Also constructing the related Green's functions could be difficult for more complex geometries.

**Discrete Dipole Approximation (DDA)**[22]
Simply stated, a simulation area in this method is discretized into finite cells of given dipole polarizability $\alpha_m$, which has been already defined in Section 2.3 by Equation 2.32. The polarization $\mathbf{p}_m$ induced at the site $\mathbf{r}_m$ is given by the polarizability $\alpha_m$ and the total electric field $\mathbf{E}(\mathbf{r}_m)$:

$$\mathbf{p}_m = \alpha_m \mathbf{E}_m. \tag{5.3}$$

where the total electric field can be expressed as a superposition of the source originated field $\mathbf{E}_{m;\mathrm{src}}$ and the dipole field $\mathbf{E}_{m,n}$:

$$\mathbf{E}_m = \mathbf{E}_{m;\mathrm{src}} + \sum_{n \neq m} \mathbf{E}_{m,n}. \tag{5.4}$$

DDA method allows to calculate the scattering of metallic structures surrounded by homogeneous media which is a major limitation for plasmonics. DDA is also a frequency-domain technique and can easily treat arbitrary material dispersion. GDM is equivalent to DDA for the low frequency limit. Similar mesh refinement as for GDM is required for complex geometry structures.

**Boundary Element Method (BEM)**[23]
BEM is far more known from physical branches as acoustics, biomechanics, etc., but it was also successfully used for solving micro-optical problems. This method is similar to GDM since it calculates the total field using incident and scattered fields. Unlike GDM, BEM describes the scattering structure by its surface interface which is then discretized. BEM calculates the total field using Equation 2.5 which is homogeneous in the region of scattering structure and inhomogeneous due to the presence of excitation field in the outer region:

$$\begin{aligned} \left(\nabla^2 + k_\mathrm{s}^2\right) \mathbf{E}_{\mathrm{tot;s}} &= 0, \\ \left(\nabla^2 + k_\mathrm{o}^2\right) \mathbf{E}_{\mathrm{tot;o}} &= \mathbf{E}_{\mathrm{src}}, \end{aligned} \tag{5.5}$$

where $k$ is the wavenumber in the structure s and in the outer region o, respectively. BEM solves boundary integral equations obtained from previous equations by applying Green's second identity and sum the contour and surface terms. This process is far beyond the scope of this thesis, detailed derivation can be found in [24].

Boundary integral equations can be arranged into a system of linear equations and solved numerically to get the scattered field. The total field is obtained as a superposition of excitation and scattered field.

**Finite-Difference in Frequency-Domain (FDFD)**
In the FDFD finite differences are used to approximate derivatives in differential equations. This procedure is described in Section 5.1 in more details. Here we discretize three coupled scalar partial differential equations which we obtained from the wave equation 2.4 [25, p. 176]. It turns into the system of linear equations (as in the case of GDM). In FDFD, we obtain a very sparse matrix system, whereas in GDM the matrix

system is dense. Consequently, FDFD solves problems more efficiently even though the entire simulation region has to be discretized. FDFD does not require Green's function and is more versatile.

To sum up, all frequency-domain methods can easily treat dispersion media. On the other hand simulation of more complex geometries is very hard. Also large number of single-frequency simulations is required to obtain broadband frequency response of simulated system. This could be overcome by computation done in the time domain where the entire frequency response is obtained in only one simulation run. So far the most used method combines discretization of space and time and is known as FDTD.

## 5.1 FDTD fundamentals

FDTD method directly solves Maxwell's curl equations 1.3 and 1.4. Both equations contain electric and magnetic quantities which implies that FDTD solves these two fields at the same time. As stated in Chapter 1, Maxwell equations have to be supplemented by material relations (1.7 and 1.8). Not only time but also space, have to be discretized in simulation to convert a continuous problem into a discrete one. Derivatives in the Maxwell equations are approximated by finite central differences. If we consider Taylor's series expansion of $f(x)$ about the spatial point $x_0 \pm \Delta x$ we get [25, p. 175]:

$$\left.\frac{df}{dx}\right|_{x_0} = \frac{f(x_0 + \Delta x) - f(x_0 - \Delta x)}{2\Delta x} + O[(\Delta x)^2], \tag{5.6}$$

where $O[(\Delta x)^2]$ represents the remainder term and $\Delta x$ corresponds to the step size. The remainder term is an error of approximation. Here it is proportional to $\Delta x^2$; therefore, the error of the approximation approaches zero as $\Delta x^2$. Therefore, our approximation given by Equation 5.6 is second-order accurate [26, p. 4]. Commonly, we divide a simulation area into rectangular cells with a grid of nodes. For given field component at the nodal point $\mathbf{r}_{ijk} = (x_i, y_j, z_k)$ Equation 5.6 becomes:

$$\left.\frac{df}{dx}\right|_i \sim \frac{f_{i+1} - f_{i-1}}{2\Delta x}. \tag{5.7}$$

For time discretization the Yee algorithm uses an arrangement where $\mathbf{E}(t = n\Delta t)$ is calculated using $\mathbf{H}(t = n\Delta t - \frac{\Delta t}{2})$, then $\mathbf{H}(t = n\Delta t + \frac{\Delta t}{2})$ is calculated using $\mathbf{E}(t = n\Delta t)$, etc. Such computational scheme is known as leapfrog arrangement and it yields central difference in time.

Spatial discretization, as well as time discretization, are second-order accurate because we use the central difference to approximate all derivatives. Spatial field component distribution is based on the Yee cell (Figure 5.1), where every **H** component adjoins four **E** components and vice versa. Following equations show discretization in detail:

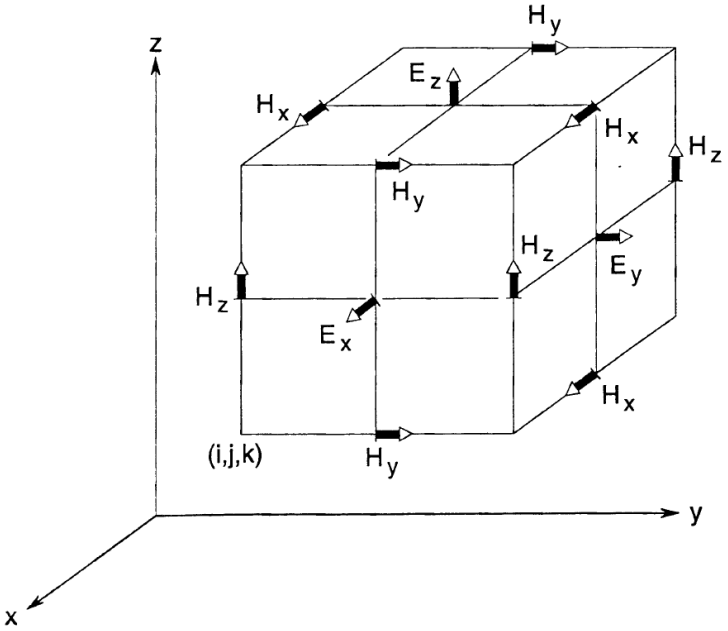


Figure 5.1: Fundamental element of Yee algorithm. It shows position of six field vector components. Every **H** component adjoin four **E** components and vice versa. Taken from [27, p. 60].

$$H_x|_{i,j,k}^{n+\frac{1}{2}} = H_x|_{i,j,k}^{n-\frac{1}{2}} +$$

$$+ \frac{\Delta t}{\mu_0}\left[\frac{(E_y|_{i,j,k+\frac{1}{2}}^{n}) - (E_y|_{i,j,k-\frac{1}{2}}^{n})}{\Delta z} - \frac{(E_z|_{i,j+\frac{1}{2},k}^{n}) - (E_z|_{i,j-\frac{1}{2},k}^{n})}{\Delta y}\right]. \tag{5.8}$$

Here the $x$-component of **H** is a sum of the $H_x$ field calculated one time step back in the same coordinates and the change of the electric field components $E_y$ and $E_z$ is calculated half of the time step before in the nearest nodes. Notice that all five field components on the right side of Equation 5.8 lie in the $yz$-plane. Similarly, all the components used for the calculation of $y$-component or $z$-component lie in the $xz$ plane or $xy$ plane, respectively.

In contrast to all frequency-domain calculation techniques, we have to derive a procedure treating dispersive materials. In these material **E** and **D** are related by constitutive relation 1.7. Auxiliary Differential Equation (ADE) [27, p. 246] is frequently used. In this method, inverse Fourier transform is applied to mentioned constitutive relation turning it into the time-domain equation relating the same quantities. Derivatives are again approximated by the central difference. During one computational step **D** is obtained from **H** first, and then **E** is obtained from the auxiliary equation.
Generally speaking, treating the dispersive materials in the time domain simulations increase computational time and memory requirements but provides broadband response in single simulation run.

# 6. Simulations and Results

In this chapter, we will present our work. We have focused on the properties of plasmonic antennas supporting localized surface plasmon resonances (LSPR) at high wavelengths. These antennas can be used in high-frequency electron paramagnetic resonance (HFEPR) to enhance the measured signal. Such application is called plasmon-enhanced (PE)-HFEPR. We have studied and optimized single antennas of distinct shapes. We have also performed simulations of periodic arrays. We have found that the maximum field enhancement of almost three orders of magnitude is theoretically possible using a judiciously designed finite array of plasmonic antennas, dielectric resonator, and gold mirror. We have also found that the maximum field enhancement is rather independent of the specific antenna shape.

## 6.1 Simulation Software

In this thesis, we performed our simulations with two different software packages for electromagnetic simulations, Ansys Lumerical FDTD and SIMULIA CST Studio Suite. Both packages utilize the FDTD method. We will now describe basic properties and a simulation scheme of our simulations. The Ansys company provides huge online manual [28]. The CST Studio has similar manual but it is accessible only from the programme. Brief solver overview might be found in Reference [29].

We will start with the Lumerical interface. In the beginning, we have to define boundaries of our simulation. When appropriate geometry of objects in simulation, we can set symmetric or anti-symmetric boundary conditions. They force some of the field components to be zero and others to obey the given symmetry. Exploiting the symmetry reduces the computation time by a factor of 2 for each dimension in which the (anti)symmetric boundary conditions are applied, i.e., up to a factor of 8 for the simulation (anti)symmetric in all dimensions. In example shown in Figure 6.1 we can set anti-symmetric boundary condition to $x_{\mathrm{min}}$ and symmetric boundary condition to $y_{\mathrm{min}}$. Since we put a substrate into the simulation region we broke $z$-symmetry. Rest of the simulation area is surrounded by Perfectly Matched Layer (PML) boundary conditions which ideally absorb all radiation leaving the simulation area. If we want to simulate an infinite array we can set periodic boundary conditions (PBC).

Another essential component of the simulations is a source that represents the input power (e.g., the incident wave). Predefined sources in Lumerical include Gaussian beam source or plane wave source, for example. The Gaussian beam would be a better approximation of the real source in our case. However, it needs a simulation area

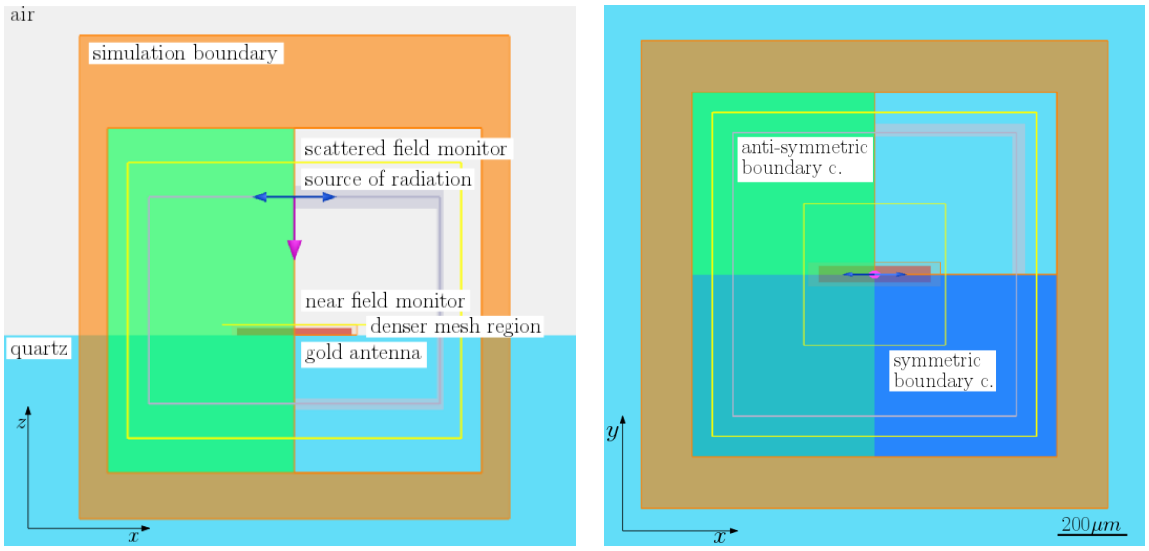


(a) (b)

Figure 6.1: Lumerical simulation scheme, (a) side view (b) top view. Scheme shows simulation of single gold antenna. Antenna dimensions are not in scale, the scale bar for all the other components is shown in (b).

to be remarkably bigger than the wavelength of the input wave. For small simulation regions, we are limited to plane wave source. In the example scheme, we used a total-field scattered-field (TFSF) source which is the plane wave source and which divides the simulation area into two regions. The inner one contains a total field (injected plane wave, field scattered by the antenna, reflected wave), whereas the outer one contains only a field scattered by the antenna. Other fields are absorbed in source boundaries marked as grey areas in Figure 6.1. Composite 2D monitor labelled as scattered field monitor then gives information about scattering properties of the antenna.

To study a magnetic field enhancement in the vicinity of the antenna, we have to employ a frequency domain monitor recording the magnetic field. Lumerical enables to create 2D or 3D monitor recording each component of the magnetic (electric) field individually. By default, the monitor is set to record the field values for $N$ frequency values equally spaced over the bandwidth of the source. Alternatively, linear wavelength spacing can be set. In Lumerical, the field values are stored in non-compressed format thus no consecutive computational proceeding is necessary to visualize or process the field values.

Due to the fast decay of the magnetic field in the vicinity of the antenna (see Equation 2.36), the space discretization have to be adjusted. Lumerical sets mesh size according to the dielectric function of a material. If we want to locally change the mesh size, we can add a region where we define the mesh size manually. The program then rearranges surrounding cells size. An analogous procedure could be done to make mesh coarser. It is typical for high wavelengths where the dielectric function of gold is very high and automatically designed mesh is too dense.

A typical scheme of simulation done in CST Studio is shown in Figure 6.2. We can choose the same boundary conditions and source types as in Lumerical. Since we

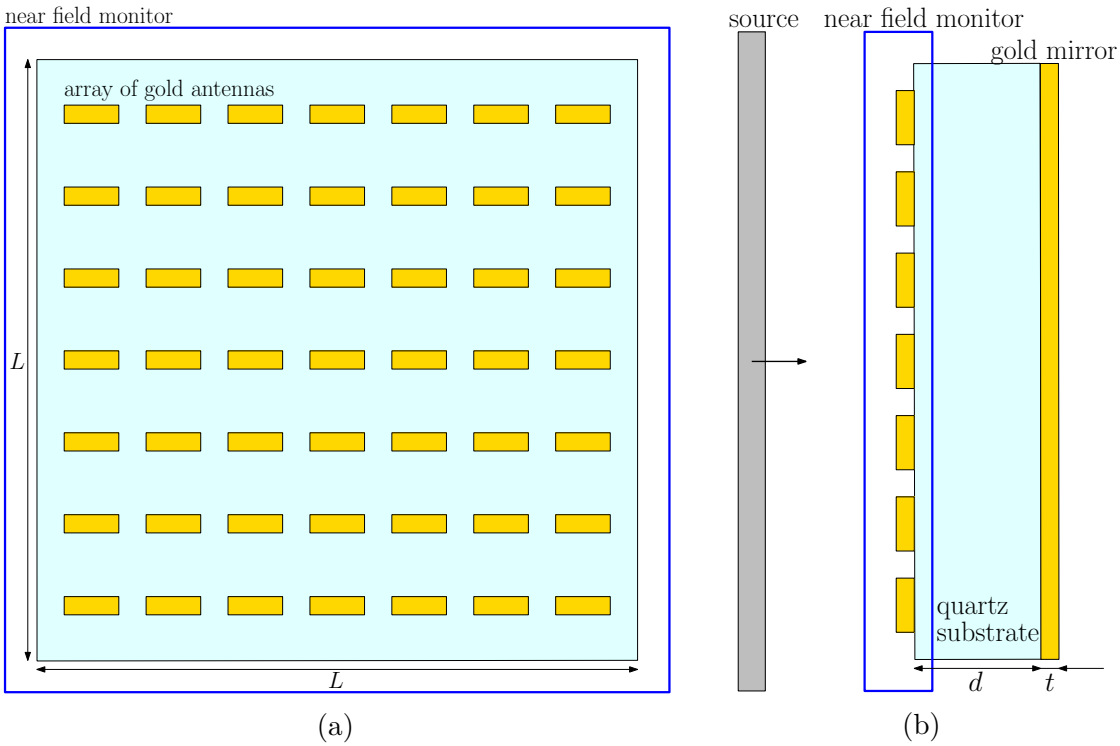


Figure 6.2: CST simulation scheme, (a) top view (b) side view. Scheme shows simulation of $7 \times 7$ array of gold antennas on finite dimension substrate with gold mirror. Scheme not in scale.

want the CST simulation to be as similar as possible to real sample, we use a Gaussian beam source with the diameter of 1.5 mm at the maximum wavelength and amplitude of $1\,\mathrm{Vm}^{-1}$ in the centre of the beam. A substrate has the lateral size $L = 3\,\mathrm{mm}$ and the thickness $d = 0.52\,\mathrm{mm}$. There is a gold mirror with the thickness $t = 200\,\mathrm{nm}$ at the bottom side of the substrate. The blue boxes in Figure 6.2 indicate boundaries of the 3D magnetic field monitor which records near field of antennas.

A major difference between the two programmes is in a way how they record and treat data from field monitors. In CST Studio user can easily cover the frequency band non-linearly. It allows a very precise simulation of structures with high quality factor (Q-factor). To obtain the same frequency resolution in Lumerical more computer memory have to be used. Once the simulation is done, CST stores field data in *.m3d* and *.s3d* format. The main advantage of this approach is the reduced memory requirements. On the other hand, the data have to be reconstructed before we start any post-processing or export procedure. Here we have to stress out that CST ignores mesh points used during the computation and reconstruct the field values in equally spaced points. Therefore, the effect of better accuracy given by mesh dense mainly applies only during computation. The size of a file containing the exported field values is also very big. A good trade-off between time, size of the file, and accuracy is to use spatial sampling ca. twice bigger than the smallest mesh size. Unfortunately, spatial sampling can not be adjusted in different direction thus square (cubic in 3D) point pattern is always made.

Irrespective of the specific data treatment, the quantity $E$ describing an enhancement of magnetic component of the wave and possible enhancement of the HFEPR signal, is from now on referred to as (magnetic) field enhancement and is given by:

$$E = \frac{|H_{iP}^2|}{|H_0^2|}, \tag{6.1}$$

where $H_{iP}$ is the magnetic field in-plane of the substrate and $H_0$ is the power source value.

## 6.2 Material properties

The theoretical description of material optical properties was given in Section 1.2. In our simulation, we use only three different materials, air as an ambient material, quartz as a substrate and gold as an antenna material.

Air is a non-absorbing dielectric with the refractive index approximately equal to 1 for the entire electromagnetic spectrum. Quartz is a form of silicon dioxide with very low absorption. According to Reference [30, p. 82], its refractive index at the frequency 245 GHz is $2.1059 \pm 0.0002$ and the loss tangent is $(1.0 \pm 0.3) \cdot 10^{-4}$. Loss tangent is a ratio between the imaginary and the real part of the dielectric function [31, p. 8]. Loss tangent of quartz is small and can be neglected.

The only absorbing material in our simulation is gold. The dielectric function was obtained using the Drude model described in Section 1.3 with values of the plasma frequency $\omega_p = 1.3 \cdot 10^{16}\,\mathrm{rad \cdot s^{-1}}$, the collision frequency $\gamma = 1.1 \cdot 10^{14}\,\mathrm{rad \cdot s^{-1}}$ and $\epsilon_\infty = 1.53$ [32]. Calculated values are shown in Figure 6.3. The real part is almost constant in a given frequency range whereas the imaginary part varies a lot. Nevertheless, gold will interact with THz electromagnetic radiation as an almost perfect conductor despite the exact value of the dielectric function. It is very different from the visible or infrared region where only small change in parameters of dielectric function may result in very distinct optical properties [33].

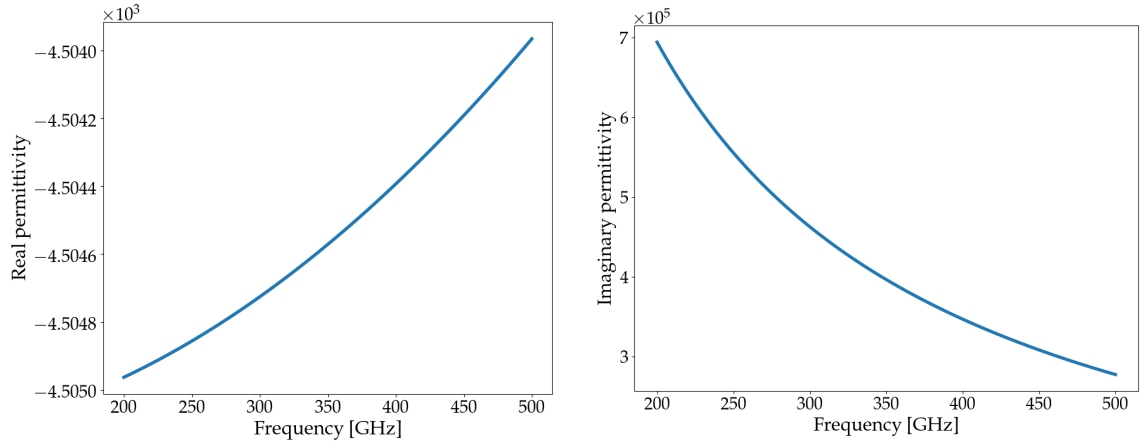


(a) (b)

Figure 6.3: Calculated real (a) and imaginary (b) part of gold dielectric function.

## 6.3 Single antennas

We start with the most simple structure: bar also referred to as rod. A single bar has only two parameters, bar length $L$ and width $W$ (Figure 6.4). Thickness of the bar was set to 0.2 µm. Magnetic field data values were taken at a height of 0.1 µm above the bar top surface and from an area of $(L + 100) \times 300\,\mu m^2$. Simulations were calculated in Lumerical using quartz substrate extending simulation area (therefore effectively semi-infinite) and PML boundary conditions. Source polarization, if not stated otherwise, is parallel to the bar length in what follows.

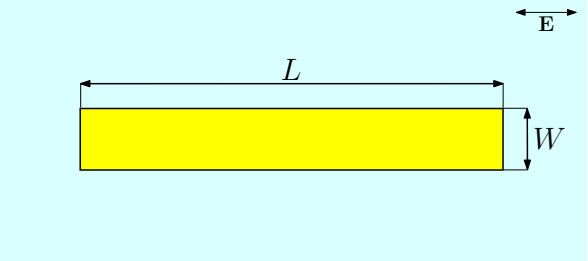


Figure 6.4: Single bar geometry. Arrow in the top right corner indicates the source polarization in following simulations.

Field enhancement produced by all single bar antenna is very low and spectrally broad (Figure 6.5). Especially for short bars, the enhancement is below 10, and Q-factor is also very low (ca. 2–3). Big separation distance (comparable to $L$) of induced charges results in a significant electric dipole moment. Consequently, the energy losses increase as the scattering becomes stronger. Broad spectrum response is a consequence of these losses.

Another frequently used plasmonic structure is a split ring which was proposed in 1999 by Pendry *et al.* [34]. Originally it consisted of two concentric rings having

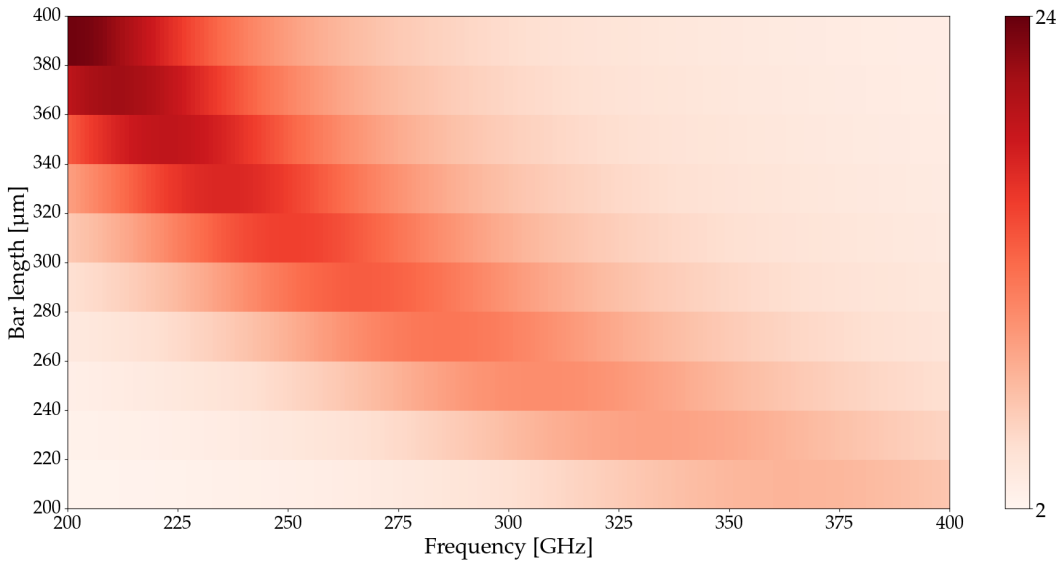


Figure 6.5: 2D map of enhancement spectra of single bar with different length. Antenna was on semi-infinite substrate. Calculated in Lumerical.

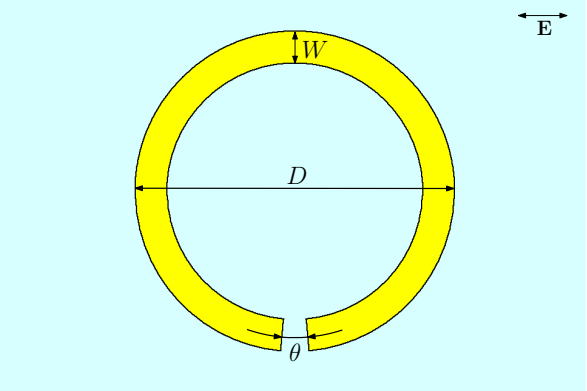


Figure 6.6: Single split ring geometry. Arrow in the top right corner indicates the source polarization in following simulations.

gaps on opposite sides. Since then, many shape modifications were done, and the split rings were already used to enhance the magnetic field in the THz region [35], [36]. The geometrical scheme of our split ring is shown in Figure 6.6. The parameters determining the shape of the split ring include the outer diameter $D$, the cut-off angle $\theta$ and the width of gold strip $W$.

Figure 6.7 shows field enhancement spectra of the single split ring on semi-infinite quartz substrate for a different combination of the diameter, the cut-off angle and the width. Magnetic field data values were taken at height of a 0.1 µm above the top surface of the split ring and from an area 300 × 300 µm$^2$ for all simulations.

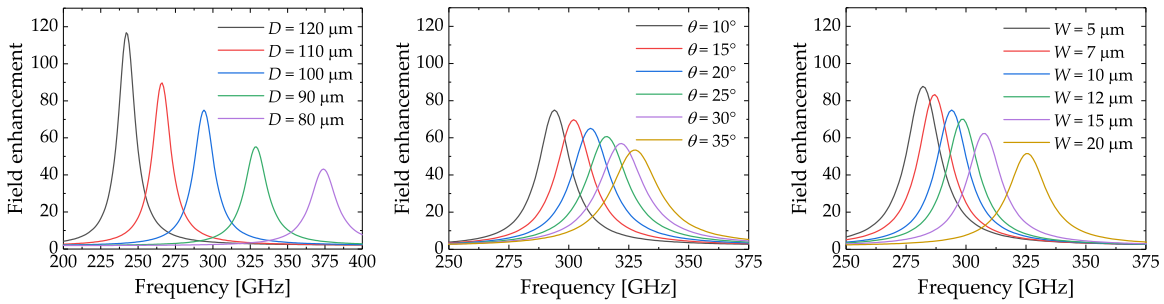


(a) (b) (c)

Figure 6.7: The enhancement spectra of the single split ring. (a) The enhancement for different diameters $D$ with $W = 10\,\mu m$ and $\theta = 10°$ kept fixed. (b) The enhancement for different cut-off angle $\theta$ with $D = 100\,\mu m$ and $W = 10\,\mu m$ kept fixed. (c) The enhancement for different $W$ with $L = 100\,\mu m$ and $\theta = 10°$ kept fixed. Calculated in Lumerical.

Figure 6.7a shows the enhancement spectra calculated for different diameters. While the maximum enhancement varies between 44 and 117, the Q-factor remains same for all the diameters and equals ca. 18. Figure 6.7b shows the enhancement spectra for $\theta$ ranging from 10° to 35°. Q-factor is decreased from 18 to 13. The effective length of the split ring given by perimeter of ring minus cutted-off part decreases which increases the resonant frequency a bit. Finally, Figure 6.7c shows the spectra for different width of the gold strip. Here the enhancement varies between 52 and 88 which is probably

due to two different contributions. The first one is associated with a change of the resonant frequency and the one second may arise from increased current density in the antenna. The current density is inversely proportional to an area through the electric current flows. In our case, the area is given by $W \times t$, where $t$ is the vertical thickness of the antenna. Resonant frequency also varies. This effect was already theoretically described using the example of a single nanorod antenna [37]. The authors have demonstrated that the resonant frequency of the rod also depends on the ratio between length and width. In our case, the ratio between diameter and width is changed, making the situation analogous. Values of the maximum enhancement as a function of resonant energy and Q-factor are shown in Figure 6.8.

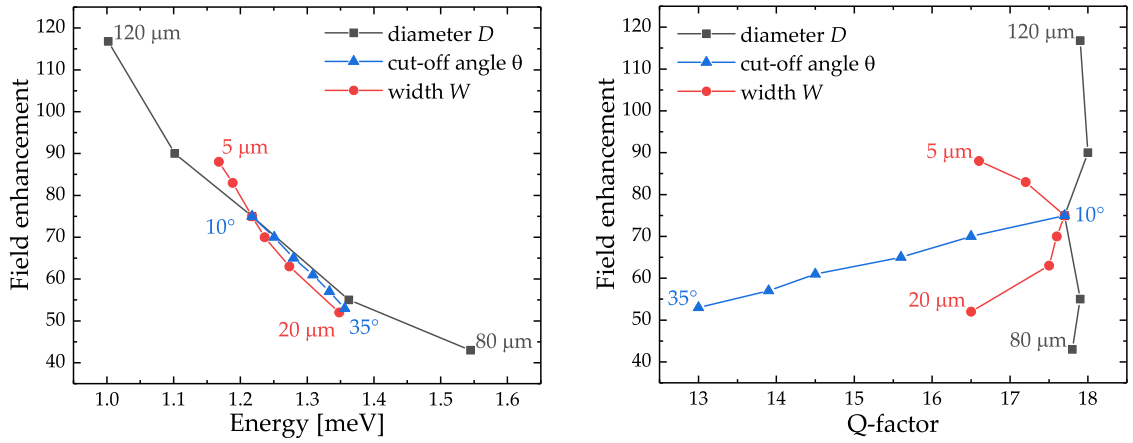


(a) (b)

Figure 6.8: Magnetic field enhancement as a function of (a) resonant energy and (b) Q-factor for all geometrical parameters of the split ring antenna. Numbers in the figures indicates span of each value line.

Figure 6.8a shows that majority of the enhancement increase is a consequence of resonant frequency change. In case of diameter dependence, a probable explanation is that split rings of bigger diameter cover a higher part of the field monitor area. In addition, the Q-factor is almost not changed (black line in Figure 6.8b). On the other hand, a higher Q-factor does not imply higher field enhancement. The Q-factor is increased a lot for smaller cut-off angle but the enhancement almost follows the diameter energy line. A significant increase of the Q-factor might be a consequence of the increased separation distance between the poles of the split ring. Similarly to the bar antenna, it affects the magnitude of the electric dipole moment which drives the scattering of the antenna. The relation between the enhancement and the Q-factor remains unclear also in case of the width of the split ring. By changing the width, the local maximum of the Q-factor is found. In contrast, the field enhancement keeps the monotone trend.

The trend of enhancement increasing with the effective length of split ring is similar to single bar simulations. However, absolute values of enhancement, as well as Q-factors, are almost an order of magnitude bigger. Top value of the enhancement exceeds 100. The highest Q-factor (18) is reached for the split rings with $\theta = 10°$ and

decrease to about 13 for $\theta = 35°$. Width of the strip reaches the maximal value of the Q-factor for $W = 10\,\mu m$. Therefore, we find this value optimal. Smaller values provide a higher value of the enhancement but could collide with spatial discretization and forces us to use smaller mesh in the following simulations.

Now we will turn our attention to the structures which have non-constant width. As we demonstrated in the example of a split ring, the change in width or missing part result in magnetic field modification. Therefore appropriately designed structures can create a segment with an enhanced electric or magnetic field. These areas are referred to as hot spots. Diabolo is an example of a structure having such magnetic hotspot in its centre (bridge) [38]. Figure 6.9 shows a comparison of magnetic field intensity

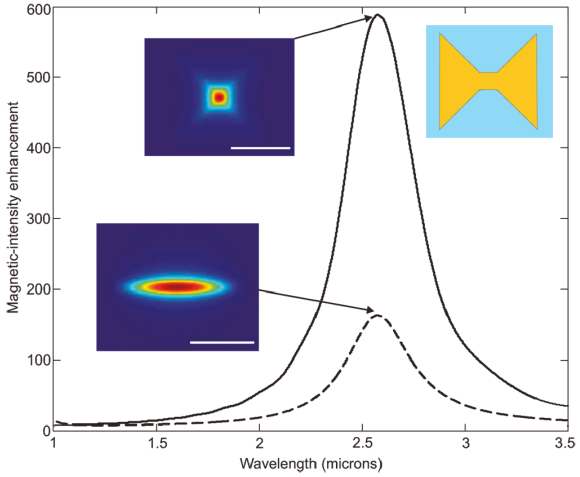


Figure 6.9: Comparison of magnetic intensity enhancement of gold diabolo antenna (solid line) and bar antenna (dashed line). Insets show the distribution of magnetic field intensity at the resonance wavelength and scheme of the diabolo geometry. The scale bar is 200 nm. Adapted from [39], edited.

of gold diabolo antenna and bar antenna. The right inset shows diabolo geometry, and the left ones show magnetic field intensity distribution for both antennas. Even though the area of strongly enhanced field in the diabolo bridge is smaller, the intensity enhancement is almost four times higher and the Q-factor of the diabolo is also better. Therefore, judiciously designed structures allow creating a hotspot concentrating and enhancing the magnetic field very efficiently.

The following structure was designed to combine magnetic field hotspot created in the bridge of diabolo antenna with high Q-factor and low lateral size provided by split ring resonator. This structure, from now on referred to as split wheel, has a complicated geometry (Figure 6.10) with many parameters at first sight. However, a majority of the parameters were already investigated in the previous part. The outer diameter $D$, the width of gold $W$ and the cut-off angle $\theta$ should have the same effects as in split ring geometry. We find sufficient to investigate an influence of diabolo angle $\delta$, width of the diabolo bridge $BW$ and length of the capacitor-like rectangles $LC$.

Figure 6.11 shows the enhancement spectra of single split wheel antenna on semi-infinite quartz substrate. For all simulation the field values were taken at height of

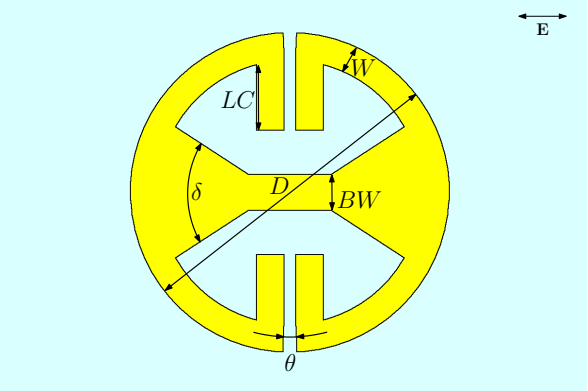


Figure 6.10: Single split wheel geometry. Arrow in the top right corner indicates the source polarization.

0.1 µm above the top surface of the split wheel and from an area of 300 × 300 µm$^2$. Parameters similar to the split ring were set to $D = 115\,\mu\text{m}$, $\theta = 10°$ and $W = 10\,\mu\text{m}$.

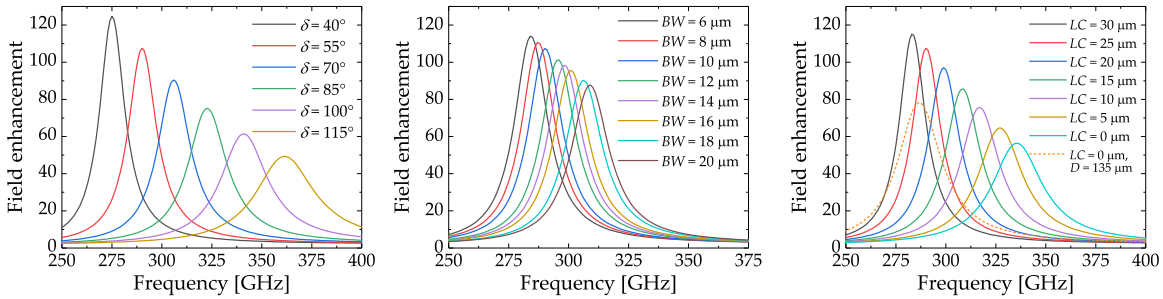


(a) (b) (c)

Figure 6.11: The enhancement spectra of the single split wheel antenna. (a) Ehancement for different diabolo angle $\delta$ with $BW = 10\,\mu\text{m}$ and $LC = 25\,\mu\text{m}$ kept fixed. (b) Enhancement for different bridge width $BW$ with $\delta = 55°$ and $LC = 25\,\mu\text{m}$ kept fixed. (c) Enhancement for different ending length $LC$ with $\delta = 55°$, $BW = 10\,\mu\text{m}$ kept fixed. Calculated in Lumerical.

In simulations shown in Figure 6.11a, the diabolo angle $\delta$ was changed while $BW$ and $LC$ were kept fixed. The spectra show that a smaller angle results in higher enhancement. The narrowest and the widest simulated antennas differ in the enhancement more than 2 times, Q-factor steeply drops and an influence of the angle on the resonant frequency is also considerable. A strength of the hotspot which is given by the bridge width increases the enhancement (Figure 6.11b). The resonant frequency is inversely proportional to the bridge width. Figure 6.11c demonstrates a possibility to tune the resonant frequency of the structure without changing the outer lateral dimensions. Both, the enhancement and Q-factor for the antenna with the largest $LC$ are almost 2 times bigger (114 vs. 58 and 17 vs. 10) than for zero $LC$. Note, that neither the enhancement nor the Q-factor difference is a consequence of better antenna properties. One contribution to the larger enhancement is because of different resonant frequency and monitor area coverage as discussed before in case of the split ring. However, the presence of the capacitor-like rectangles brings another contribution. To ensure this,

we have compared two antennas with the same resonant frequency (∼285 GHz), one with large $LC$ of 30 µm and the other with zero $LC$ and slightly enlarged diameter $D \cong 135$ µm to ensure very similar resonant frequency. The enhancement spectrum is shown in Figure 6.11c (the orange dashed line). We observed significantly worse parameters for the latter structure with the enhancement of 78 (compared to 115 in the former structure) and the Q factor of 11 (compared to 18). Figure 6.12 summarizes the values of maximum enhancement as a function of resonant energy and Q-factor.

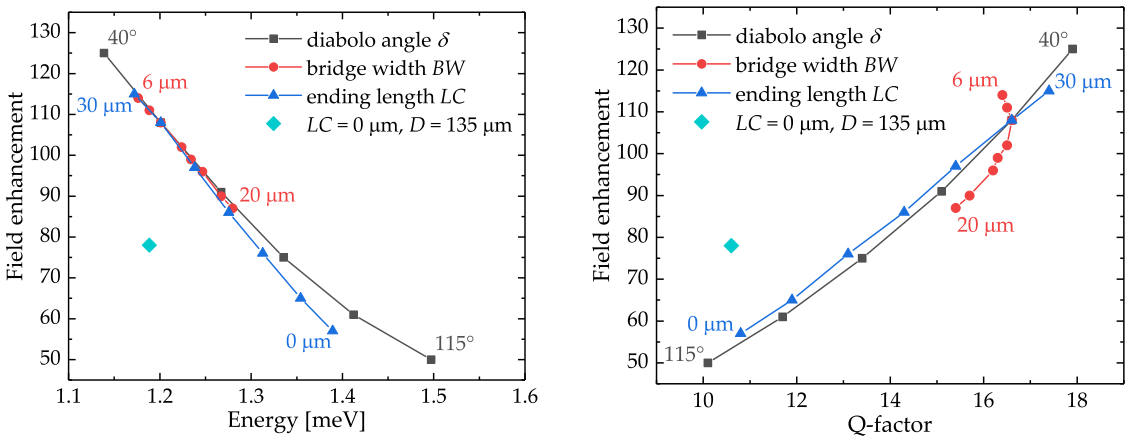


(a) (b)

Figure 6.12: The magnetic field enhancement as a function of (a) resonant energy and (b) Q-factor for some geometrical parameters of the split wheel antenna. Numbers in the figures indicates span of each value line. The cyan point represents the comparison simulation of bigger split wheel with the zero $LC$.

Now, let us do a brief comparison of all the antenna shapes we have simulated so far. We already described influence of some geometrical parameters. Figure 6.13 shows again the field enhancement as the function of energy or Q-factor. However, we will now choose only some parameters to illustrate their influence. As discussed above, the enhancement and the Q-factor of bar antennas are very low compared to the remaining shapes. At the resonant frequency 1.5 meV it is more than 5 times lower compared to the split ring. Note, that simulation of the bar antenna with length of 200 µm is the only one where the detector area was the same as for split ring and split wheel simulations. For longer bar antennas, the detector area had to be increased. Therefore, the enhancement predicted for the bar antennas was lowered. On the other hand, ratio of the detector area does not exceed 1.5 which keeps the bar antenna far behind the other two geometries. As previously mentioned, the split wheel shape is based on the split ring. Similar performance might be also seen in Figure 6.13a for split wheel with zero $LC$. On the same resonant frequency the values of the enhancement within 10 %. In such configuration of the split wheel the Q-factor is much lower compared to the split ring. This is given by the diabolo bridge which drives the scattering as discussed above. Elongation of the capacitor-like rectangles increases the Q-factor up to the value comparable with the split ring. However, at the resonant frequency 1.2 meV the

enhancement of the split ring is just over 40 % higher making the split wheel far more promising structure.

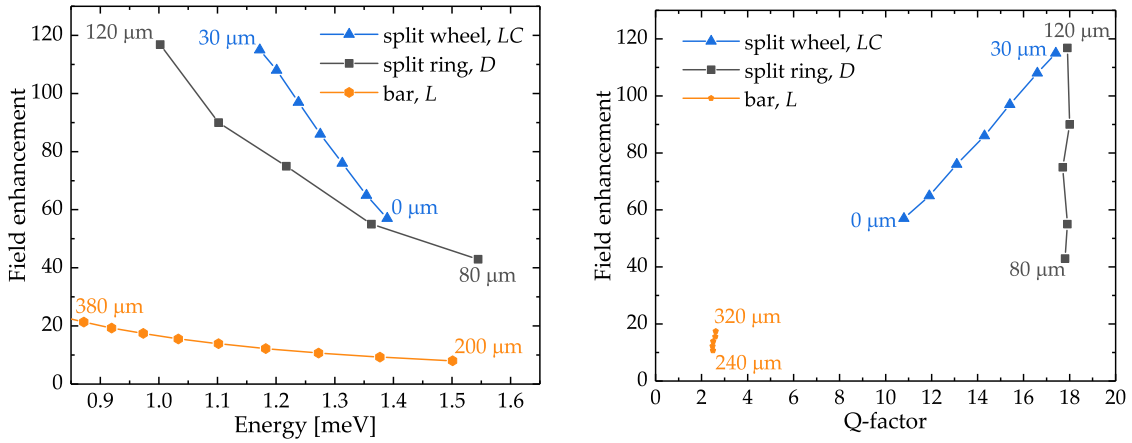


(a) (b)

Figure 6.13: The magnetic field enhancement as a function of (a) resonant energy and (b) Q-factor for one selected geometrical parameter of the given single antennas. Numbers in the figures indicates span of each value line.

Thus far, the presented results show that the magnetic field enhancement produced by single antennas without an influence of finite dimensions substrate and gold mirror is strongly dependent on the antenna geometry. Some of the parameters seem to play important role in overall enhancement and Q-factor value and some of them not. Figure 6.14 shows a comparison of the magnetic field enhancement produced in the vicinity of the antennas. These 2D maps were obtained from magnetic field data taken at a height of 0.3 µm above the substrate top side. These values were then divided by the magnetic field produced by the source. Therefore, these maps show local field enhancement at every point. Presented structures have resonant frequency near 290 GHz to eliminate the influence of higher field enhancement for lower frequencies.

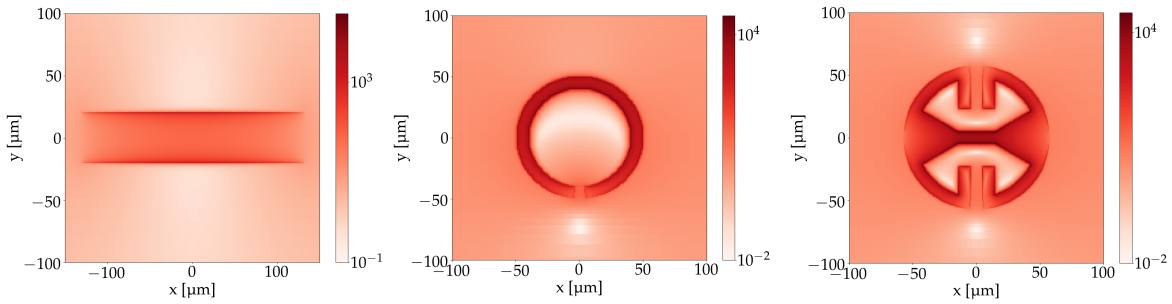


(a) (b) (c)

Figure 6.14: 2D maps of local field enhancement. (a) Bar antenna, (b) split ring and (c) split wheel. Maximum of each color bar is set to 35,000 which corresponds to maximum enhancement of the split wheel. Labels of the color bar denote the order of magnitude of minimum and maximum enhancement for every map. Calculated in Lumerical.

Maximum field enhancement produced by single bar antennas is an order of magnitude smaller than for the other two structures and does not exceed 1,300. The field produced by the split ring is the strongest at the upper part. Here the enhancement value is about 18,500. The split wheel concentrates magnetic field near its bridge and creates a well-defined hotspot with a local enhancement value reaching 35,000 above the edges of the bridge.

In the next part, we will focus on a quantitative characterization of additional magnetic field enhancement caused by finite substrate dimension and by the gold mirror. We will use the CST simulation scheme described in Section 6.1, and ELM described in Chapter 4.

## 6.4 Array of antennas

To create an array of antennas we take a single geometry and define periodicity. Figure 6.15 shows an example of the bar antenna array where $X_{\text{pitch}}$ and $Y_{\text{pitch}}$ is the distance from one centre to another in $x$ and $y$ direction, respectively. Sometimes it is more proper to think about the shortest distance between the antennas; therefore, we may define $X_{\text{gap}} = X_{\text{pitch}} - L$ and $Y_{\text{gap}} = Y_{\text{pitch}} - W$. These relations are valid for bar arrays. In case of a split ring and a split wheel antennas, analogous relations may be defined replacing $L$ and $W$ by $D$.

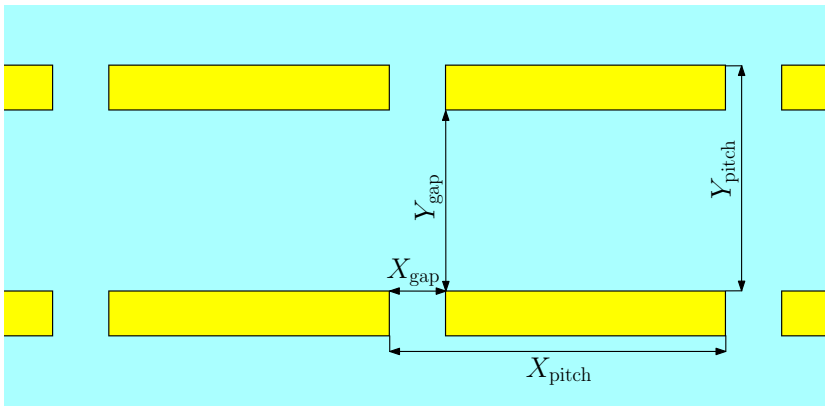


Figure 6.15: Bar array geometry.

The resonant frequency of an array of antennas changes with varying dimensions of the antenna, for example. Therefore, to investigate the magnetic field enhancement at different frequencies, the antenna length $L$ was changed. Other values were kept fixed at values $W = 40\,\mu\text{m}$, $X_{\text{gap}} = 25\,\mu\text{m}$ and $Y_{\text{pitch}} = 300\,\mu\text{m}$.

Figure 6.16 shows 2D maps of the magnetic field enhancement calculated using CST studio and ELM. In CST, an array consisting of the finite number of antennas was simulated, whereas ELM treated effectively infinite array since periodic boundary conditions were set. Both simulation sweeps show that the enhancement is getting higher and reaches the first maximum near the bar length of 270 µm (with resonance at 293 GHz). Then very steep dip is present with almost zero enhancement value for bar length 305 µm (285 GHz). The second maximum follows at the length of 345 µm (278 GHz)

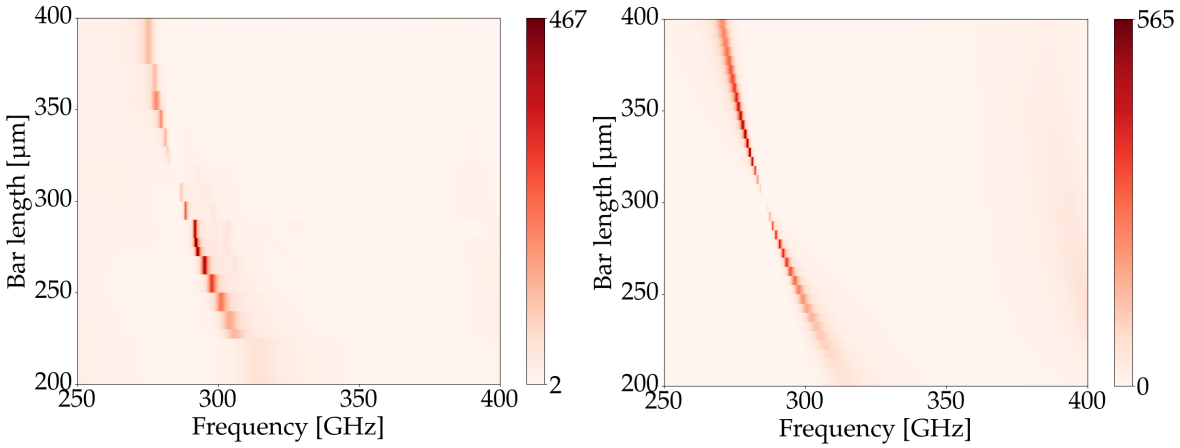


Figure 6.16: 2D map of the enhancement spectra for different bar length array. (a) CST simulations. (b) Calculated with ELM in Lumerical.

and then enhancement slowly vanishes. Q-factor of spectral peaks exceeds 200 for the largest-enhancement configurations. With full width at half maximum (FWHM) of only 1.5 GHz, this structure has an extremely sharp resonant profile. It pronouncedly differs from an individual bar (see the 2D map in Figure 6.5).

The spectral position of the maximum field enhancement obtained by CST and by ELM agree very well for shorter bars. Small difference occurs near the length of 280 µm and for lengths exceeding 330 µm. Comparison of the resonant wavelengths predicted by both models is shown in Figure 6.17a.

The magnetic field enhancement maps predicted by both programmes is shown in Figure 6.17b. It agrees very well for bar length up to ca. 280 µm. Then it started to significantly vary. In CST, splitting is strongly asymmetrical and local maxima

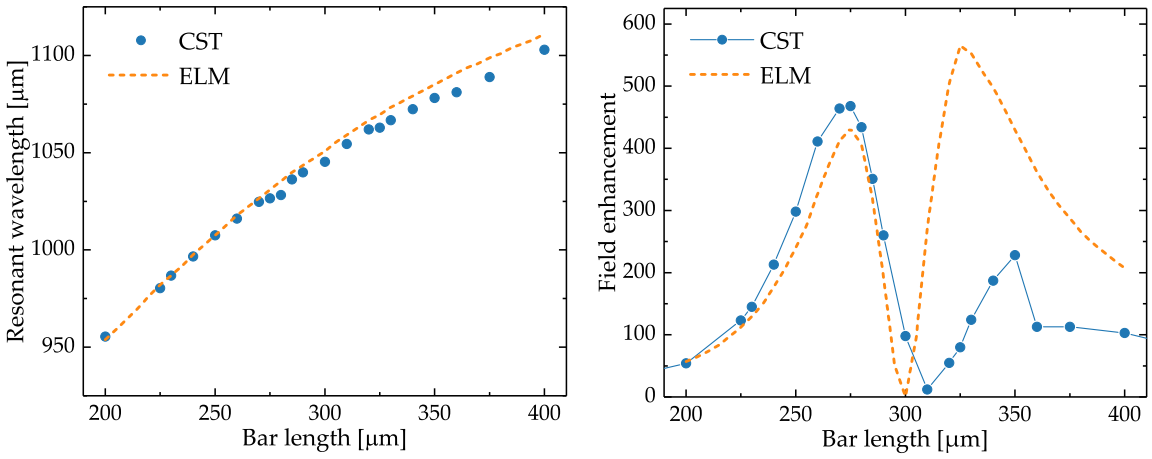


Figure 6.17: Comparison of bar length sweep results. (a) Dispersion relation obtained by CST finite array simulations (blue dots) and by ELM infinite array simulations (orange dashed line). (b) Maximum value of enhancement for every bar length. The solid blue line connection is guide for the eye.

vary by a factor of 2. According to ELM, the splitting is almost symmetrical. This difference might be due to a low number of antennas in the CST array, especially in the $x$ direction. Here their number is decreased to 5, which is far different from the infinite array which is calculated by ELM. The difference might be also related to the finite lateral dimension of the quartz substrate.

In the previous sweep, we set the distances between antennas rather deliberately. The estimation was based on a fact that we did not want any diffractive order of lattice to be present. According to [40], the lowest diffraction order appears when a critical pitch $P_c$ is reached. The critical pitch is given by: $P_c = \frac{\lambda}{n}$, where $\lambda$ is the resonant wavelength and $n$ is the substrate index of refraction. Therefore, we need to keep $X_{\text{pitch}}$ and $Y_{\text{pitch}}$ below this value. For our simulation frequency range, the $P_c$ varies between 350 µm and 570 µm.

Now we will explore an influence of the pitch size using bar antenna with $L = 275$ µm. Figure 6.18 shows 2D maps of enhancement spectra for varying $X_{\text{gap}}$ and $Y_{\text{pitch}}$.

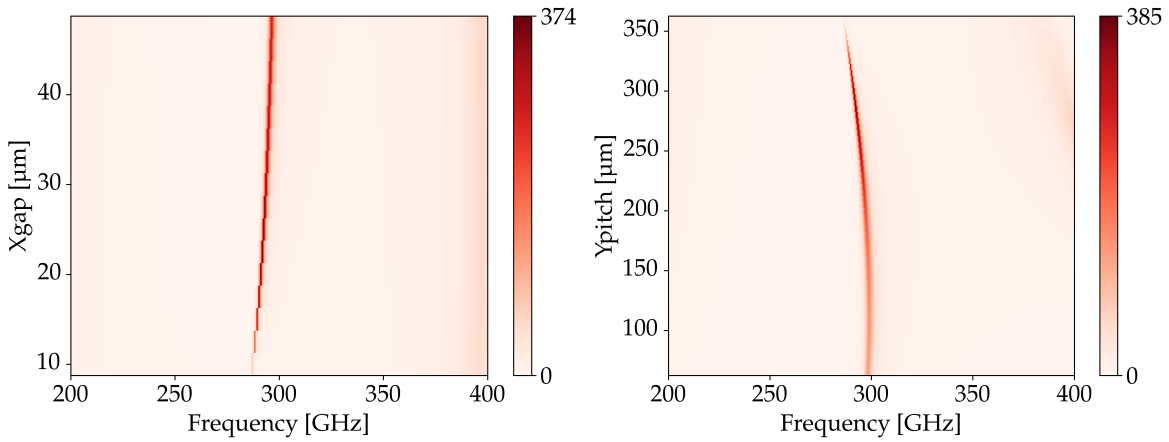


(a) (b)

Figure 6.18: Maps showing the spectral dependence of magnetic field enhancement for differenta(a) $X_{\text{gap}}$ and (b) $Y_{\text{pitch}}$. Bar dimension were 275 µm and 40 µm. $Y_{\text{pitch}}$ in panel (a) was set to 300 µm and $X_{\text{gap}}$ in panel (b) was set to 25 µm. Calculated with ELM in Lumerical.

While increasing the $X_{\text{gap}}$ and keeping $Y_{\text{pitch}} = 300$ µm, the enhancement rapidly increases from an initial value of 90 to the maximal value 374 for $X_{\text{gap}} = 22.5$ µm. Here, an extremely sharp resonance peak with Q $\geq$ 200 and central (resonant) frequency 291.75 GHz is formed. For larger separation distance the field enhancement slowly decreases and the resonant peak becomes broader. For $X_{\text{gap}} = 50$ µm the enhancement is 270 and the peak has Q = 120 with a central frequency 296.5 GHz (Figure 6.18a). Difference of almost 5 GHz in the resonant frequency origins from near field interaction of the antennas. This phenomenon was intensively studied at plasmonic antennas with the resonant wavelength in visible part of the spectrum. There, smaller distance between the antennas causes an increase or decrease of the resonant wavelength which is demonstrated by a colour change of emitted light. Therefore, this phenomenon is referred to as red-shift or blue-shift [41], [42]. In Figure 6.18a, we can observe the

red-shift. $Y_{\text{pitch}}$ dependence is shown in Figure 6.18b, $X_{\text{gap}} = 22.5\,\mu\text{m}$. We started at a value of 60 µm where the resonant frequency is 298.25 GHz, the Q-factor is 90, and the enhancement is 130. Optimum performance of array is reached for $Y_{\text{pitch}} = 290\,\mu\text{m}$. Here the values of enhancement and Q-factor are almost the same as for $X_{\text{gap}}$ sweep. Blue-shift is present for short $Y_{\text{pitch}}$ distances. Note that difference of few per cent in predicted values of the enhancement may occur as the antenna discretization and mesh density vary a bit.

Now we turn our attention to the arrays of split rings. At first, we will sweep the outer diameter while both pitches remain constant. We take $X_{\text{pitch}} = Y_{\text{pitch}} = 300\,\mu\text{m}$ as the starting point since it was nearly the optimum value for bar arrays.

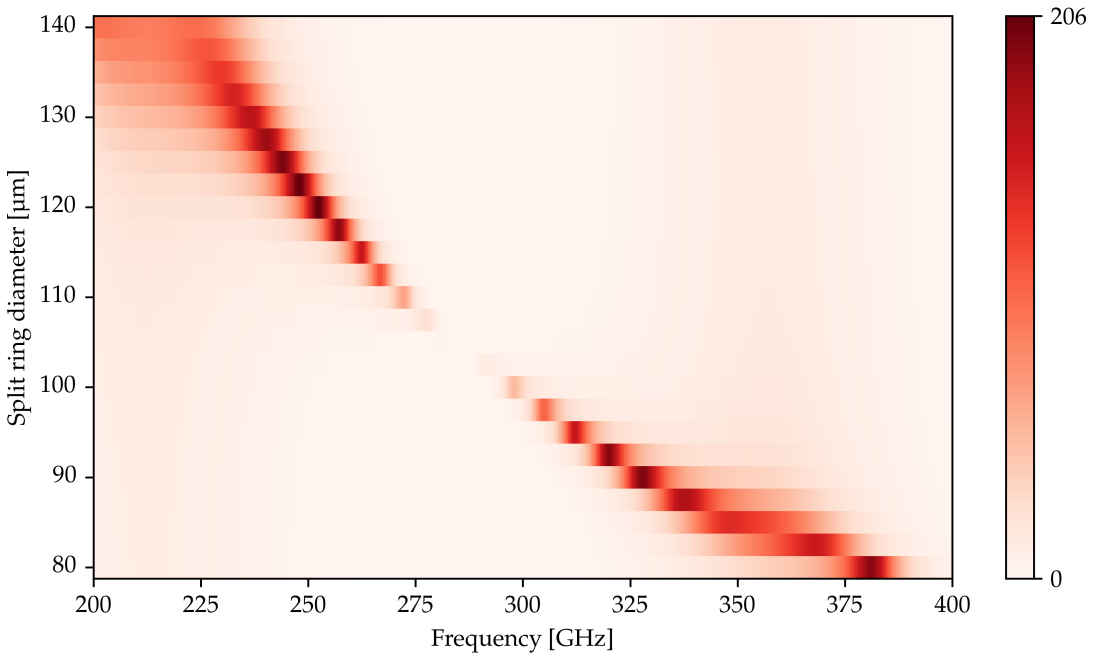


Figure 6.19: 2D enhancement map of the split ring diameter sweep. Pitches were kept fixed at the value of $X_{\text{pitch}} = Y_{\text{pitch}} = 300\,\mu\text{m}$. Calculated with ELM in Lumerical.

The enhancement spectra for split rings of different diameters are shown in Figure 6.19. Split rings with the diameter between 80 µm and 90 µm have an asymmetric peak. The peak of split rings with the resonant frequency slightly higher than 350 GHz is asymmetric towards lower frequencies and vice versa. In other words, some enhancement that does not originate only from the antennas itself occurs near this frequency. Then dip with zero enhancement is present at the frequency of 285 GHz, which is identical with the bar antennas array response (Figure 6.16b). Spectra of bigger split rings become narrow near the frequency of 250 GHz and all of them are asymmetrical towards lower frequencies again. The biggest enhancement provides a split ring with the diameter of 120 µm, the peak value is 206 and the Q-factor is 35. In the region above enhancement dip, similar values (peak 192 and Q-factor 42) are achieved for a split ring with the diameter of 92.5 µm, and with the resonant frequency 320 GHz. Since the values of both split rings are very similar, we choose the smaller split ring with a higher Q-factor for the following simulations.

Figure 6.20 shows results of pitch sweeps of an infinite split ring array calculated with ELM in Lumerical. First, the $X_{\text{pitch}}$ was varied while $Y_{\text{pitch}}$ was kept fixed with the

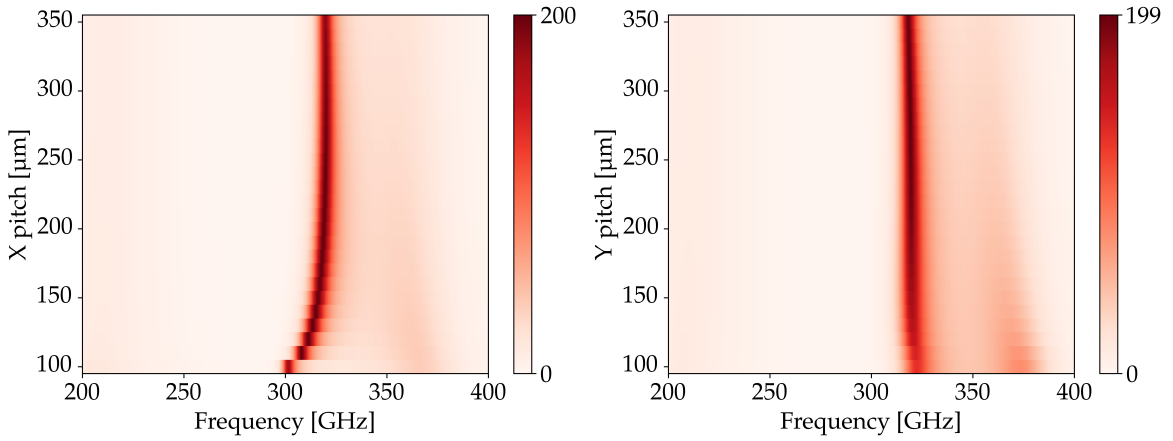


(a) (b)

Figure 6.20: 2D map of enhancement spectra of split ring array for different (a) $X_{\text{pitch}}$ and (b) $Y_{\text{pitch}}$. Split ring diameter was 92.5 µm. $Y_{\text{pitch}}$ in (a) was set to 300 µm and $X_{\text{pitch}}$ in (b) was set to 200 µm. Calculated with ELM in Lumerical.

value equal to 300 µm. The 2D map of enhancement spectra is shown in Figure 6.20a. Obtained field enhancement shows no significant dependence on the distance in $x$ direction. Only for very close spacing it decreases and the resonant frequency is red-shifted. For $X_{\text{pitch}}$ in range between 120 µm and 240 µm, the enhancement value is ca. 200 and then starts slowly decreasing (185 for $X_{\text{pitch}} = 240$ µm). We choose a value of 200 µm to perform $Y_{\text{pitch}}$ sweep. In this batch of simulations, we see more remarkable dependence. For very close spacing the enhancement reaches values below 140. The maximum value occurs for $Y_{\text{pitch}} = 280$ µm. Maximum value of enhancement is almost the same as in case od the diameter sweep where both pitches were set to 300 µm. The Q-factor remains almost the same also. Here it is 37 with the central frequency 317 GHz.

Finally, we will repeat the same procedure as before, now for split wheel arrays. Figure 6.21 shows 2D map of enhancement spectra for different diameter. Both pitches were set to 300 µm again. The trend of the enhancement increasing and decreasing is identical to split ring. The dip with almost zero enhancement occurs near 285 GHz. Below this frequency, a split wheel with the diameter of 155 µm dominates. The maximum calculated enhancement is 205, reached at the frequency of 248 GHz, and the Q-factor is 35.

The sweeps of $X_{\text{pitch}}$ and $Y_{\text{pitch}}$ show no significant dependence of the magnetic field enhancement (Figure 6.22). Only for very close spacings, where the resonant frequency is red-shifted or blue-shifted, the enhancement decreases. For $X_{\text{pitch}}$, the enhancement exceeds value of 200 for pitches larger than 200 µm (Figure 6.22a). In case of $Y_{\text{pitch}}$, the same statement is valid for the pitch larger than 230 µm.

In general, predicted values of the enhancement and the Q-factors are much lower in comparison to the bar arrays. Compared to the single antenna simulations the enhancement and the Q-factor of bar antenna arrays were increased by almost two

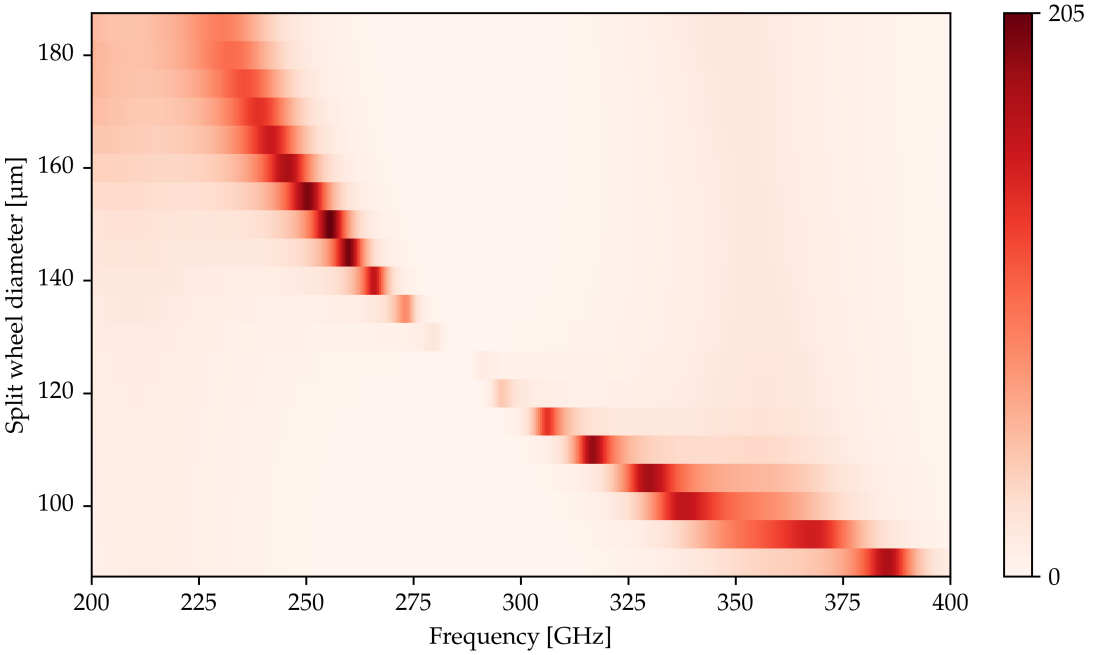


Figure 6.21: 2D enhancement map of split wheel diameter sweep. Pitches were kept fixed at the value of $X_{\text{pitch}} = Y_{\text{pitch}} = 300\,\mu\text{m}$. Calculated with ELM in Lumerical.

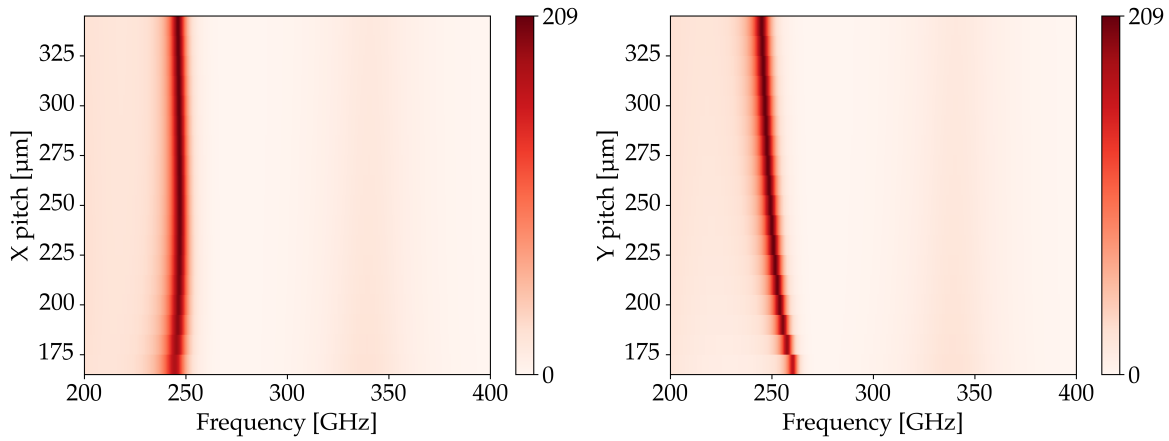


(a) (b)

Figure 6.22: 2D map of enhancement spectra of split wheel array for different (a) $X_{\text{pitch}}$ and (b) $Y_{\text{pitch}}$. The split wheel diameter was 155 µm. $Y_{\text{pitch}}$ in (a) was set to 300 µm and $X_{\text{pitch}}$ in (b) was set to the same value. Calculated with ELM in Lumerical.

orders of magnitude whereas for the split ring and split wheel the ELM predicts a rise of the observed values by a factor of ca. 2. The values of enhancement and Q-factor strongly depends on frequency. Therefore let us now turn to an analysis of the ELM to see how the substrate and the gold mirror affect antennas and vice versa. We will use data from the split ring diameter sweep.

At first we remind Equation 4.6 which describes the enhancement factor:

$$\frac{p(\omega)}{p_0(\omega)} = \frac{1 + \frac{r_{12}+r_{23}e^{2ik_2d}}{1-r_{21}r_{23}e^{2ik_2d}}}{1 + \frac{E^{\downarrow}}{1-r_{12}} \frac{t_{21}r_{23}e^{2ik_2d}}{1+r_{21}r_{23}e^{2ik_2d}}}. \tag{6.2}$$

This relation has many input parameters and is quite complicated. Figure 6.23 shows the frequency response of the substrate and gold mirror together with enhancement produced by the antennas. Altogether this makes a very complex system.

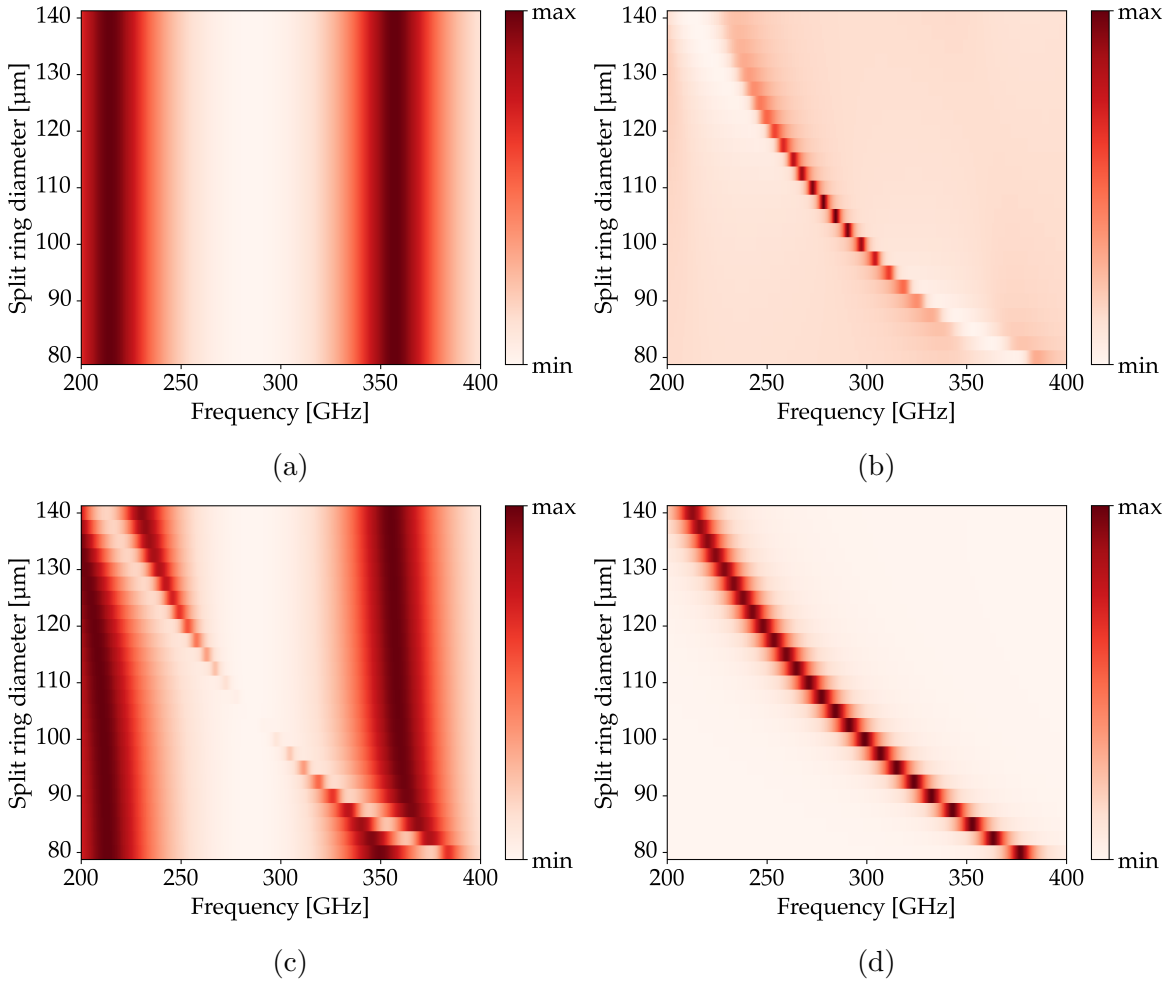


Figure 6.23: The analysis of the enhancement origin in ELM model shown on the example of the split ring diameter sweep. (a) The second power of the absolute value of the numerator in Equation 6.2 and panel (b) shows the same but for the inverse value of the denominator. (c) The second power of the absolute value of the enhancement factor is plotted. (d) Magnetic field enhancement produced by the antennas. Each colour bar is normalized to its maximum and minimum.

Figure 6.23a shows the second power of the absolute value of the numerator in Equation 6.2. It describes the effective reflection properties of the substrate and the gold mirror. What stands out is periodicity represented by two maxima, one is at the frequency of 214 GHz, and the second one at 357 GHz. Symmetrically between them,

the minimum is present at 285.5 GHz. Let us turn our attention to the denominator of Equation 6.2. Its inverse value of the second power of absolute values is plotted in Figure 6.23b. This term already contains a contribution of the antennas in the amplitude of the downward emitted wave $E^{\downarrow}$. The term is maximal for frequency 284 GHz and D=105 µm. Note that enhancement dip is present at these coordinates for the final map (Figure 6.19).

So far, we have investigated only the amplitude of the enhancement factor. However, the numerator and the denominator are complex numbers, and phase matching between them also has to be analysed. Figure 6.23c shows the second power of the enhancement factor. The minimum of the enhancement corresponds to the maximum of the denominator. Moreover, it reveals a decrease of the enhancement factor at the frequencies where the resonance of split ring antennas occurs. This position can be clearly seen in Figure 6.23d, where magnetic field enhancement is plotted. By multiplying these values with values of enhancement factor (Figure 6.23c) we will get the final 2D map of magnetic field enhancement produced by a particular antenna infinite array. In this case, the map would be identical to that in Figure 6.19.

The previous part has shown that the magnetic field enhancement produced by an array of antennas strongly depends on matching the phase of wave emitted by antennas with the phase of the wave which is reflected in the substrate. In ELM, the response of the substrate is given by a Fabry-Pérot resonance which is fixed in this model and could not be affected by antennas emitted wave. This assumption might not be valid and results obtained with this model have to be interpreted with caution. On the other hand, a simplicity and low computational demands of this method together with very good agreement with CST simulation of bar arrays (Figures 6.16 and 6.17) indicate that ELM might be used for preliminary calculations and optimizations.

Based on these preliminary calculations, we have performed a few simulations of a finite size array of the split ring and the split wheel antennas placed on the quartz substrate with the gold mirror at the bottom side. In CST, the best values of enhancement were reached for a split ring with the diameter D = 95 µm (Figure 6.24). The ELM assumption was D = 92.5 µm. The spectrum which is marked by a green line corresponds to a configuration with almost zero enhancement.

Figure 6.25 shows the enhancement spectra for different $X_{\text{pitch}}$ and $Y_{\text{pitch}}$. The diameter of a split ring was kept at 95 µm. Simulated bandwidth varied from 250 GHz to 400 GHz and the figure shows detail of the spectra only.

The spectra show no significant change in the enhancement for the pitch values between 200 µm and 350 µm which is again in good agreement with the results of the ELM. The field enhancement varies between 630 and 750, with the only exception of an array with the $X_{\text{pitch}} = 300$ µm and $Y_{\text{pitch}} = 150$ µm (light green line in Figure 6.25b). Smaller pitches enable to put more antennas on the substrate and higher its coverage. In the simulations where one of the pitch was equal to 150 µm, an array consisting of $13 \times 7$ antennas was calculated. Even though the number of antennas was almost double, the enhancement did not exceed 700. It suggest that higher coverage of the sample with the antennas does not provide any significant increase of the field enhancement.

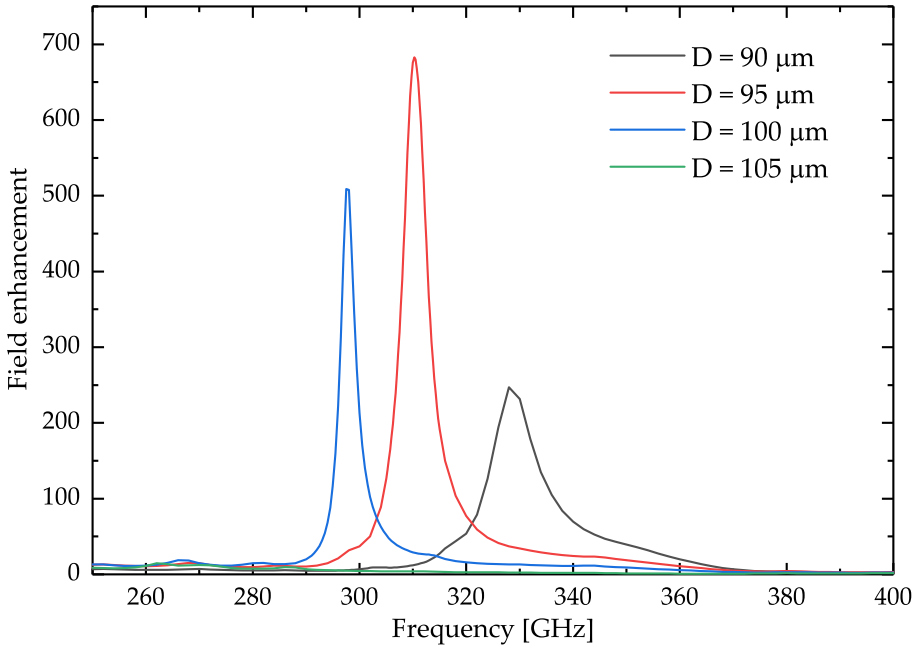


Figure 6.24: The field enhancement spectra of split ring diameter sweep, $X_{\text{pitch}} = Y_{\text{pitch}} = 300\,\mu\text{m}$ was kept. Calculated in CST studio.

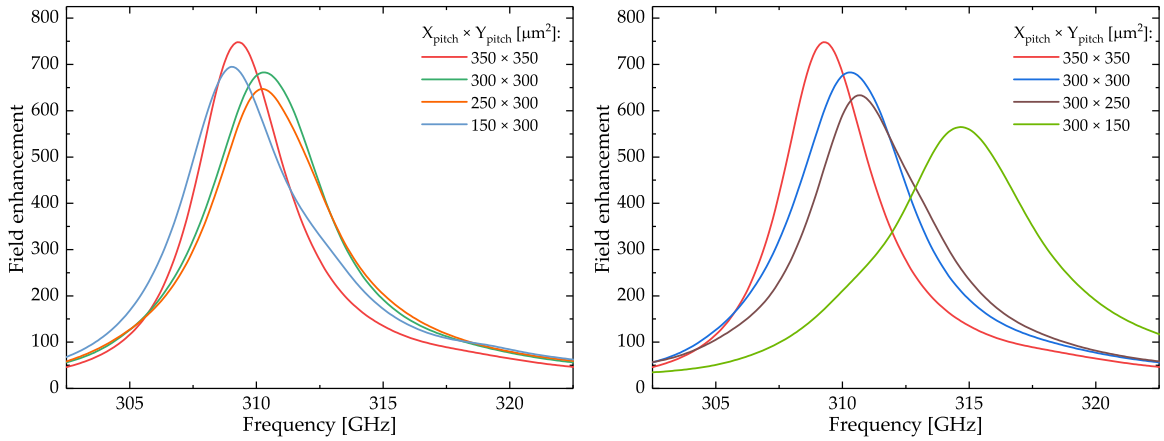


(a) (b)

Figure 6.25: Detail of the enhancement spectra for different $X_{\text{pitch}}$ and $Y_{\text{pitch}}$. The red lines in both panels correspond to the same pitch distances.

Finally, Figure 6.26 shows the enhancement spectra for $7 \times 7$ array of split wheels with different diameter. $X_{\text{pitch}}$ and $Y_{\text{pitch}}$ were kept at a value of 250 µm. The enhancement spectra follow the same trend as in ELM simulations. For smaller diameters, the peak is broadened and asymmetric with a steeper slope towards lower frequencies . We achieved the best enhancement with the diameter of 105 µm ($D = 110\,\mu\text{m}$ had been predicted by ELM).

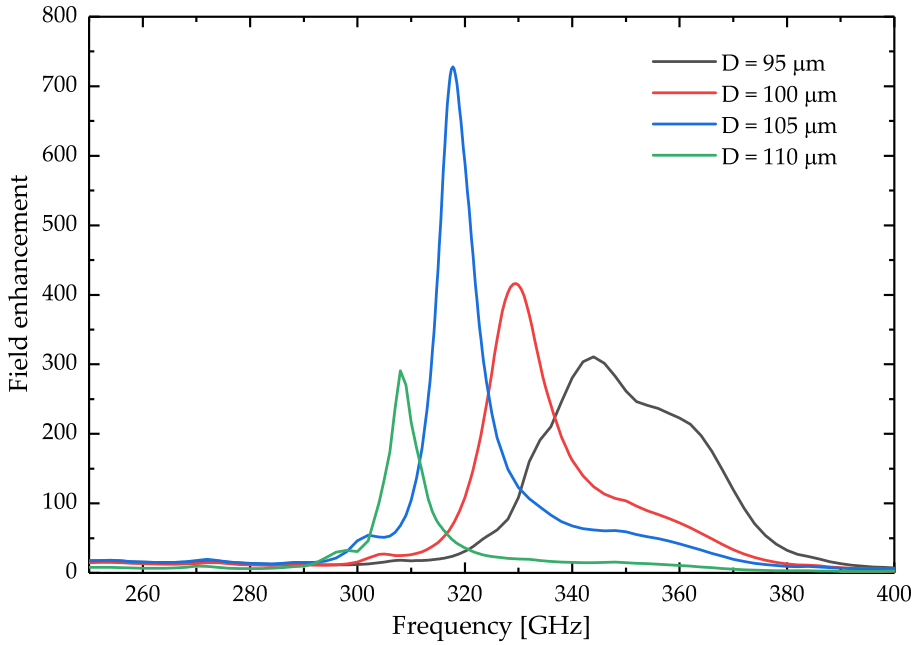


Figure 6.26: The field enhancement spectra of split wheel diameter sweep, $X_{\text{pitch}} = Y_{\text{pitch}} = 250\,\mu\text{m}$. Calculated in CST studio.

Spectra with the best enhancement among those discussed so far are shown in Figure 6.27. For a bar antenna, we predicted the enhancement of 470 and the Q-factor bigger than 200 at the frequency of 292.25 GHz. Even higher enhancement may be provided by a split wheel resonator (730). This structure has a low Q-factor which

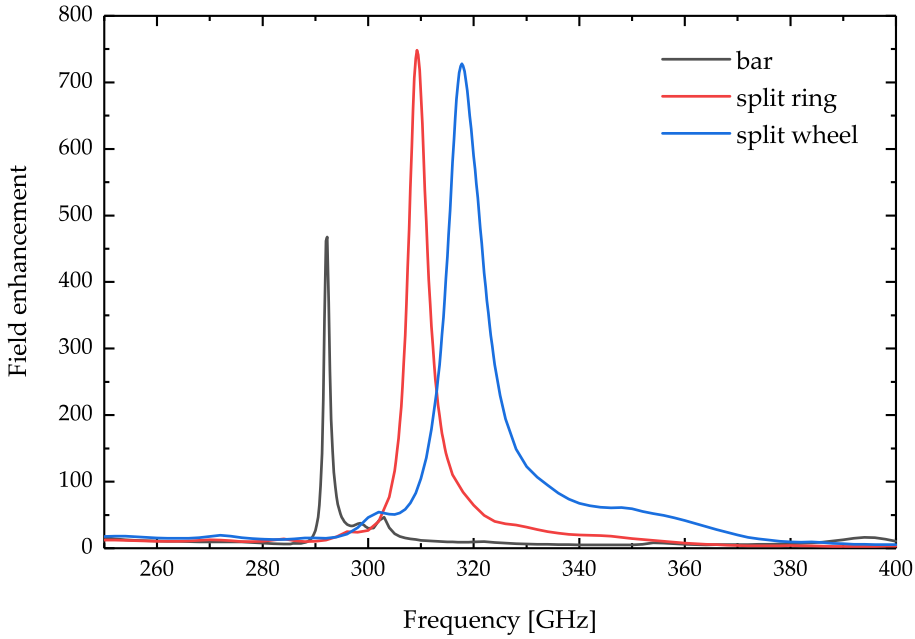


Figure 6.27: Magnetic field enhancement spectra with best peak value for different geometries. Finite array of the antennas was calculated and field values were averaged over the entire substrate area at height of 0.4 µm.

is equal to 40, and the resonance is at 318 GHz. Finally, the highest value of the enhancement was reached by a split ring. It has a peak value of 750, and the Q-factor is 70 with the resonant frequency near 309.5 GHz.

Figure 6.28 shows the distribution of in-plane magnetic field in the vicinity of antennas. These values were obtained from CST simulation of finite antenna arrays. We took the data from an area of $300 \times 300\,\mu m^2$ at the height of 0.4 µm above the substrate's top side. Although the average enhancement of all the antennas presented in Figure 6.27 is in the same order of magnitude, the magnetic field distribution is very different for the bar and the other two structures. The difference comes out from the formation of the magnetic field hotspot in the latter two structures. A major contribution to average enhancement produced by the split wheel is given by the presence of only 0.24 % of pixels with an enhancement value bigger than $10^5$. In contrast, enhancement in 86 % of pixels does not exceed the value of 100 (Figure 6.28f). These numbers are similar to the split ring where 89.5% of pixels is under enhancement 100 and 0.75 % exceed $10^5$ (Figure 6.28e). However, field distribution is dramatically different for the bar antenna. The histogram in Figure 6.28d shows that 84.5 % pixels belong to the bin with the enhancement between $10^2$ and $10^3$. 13.5 % of pixels exhibits the enhancement above $10^3$. Finally, the remaining 2 % of pixels exhibits the enhancement lower than 1. These pixels reduce the overall value of the enhancement a lot.

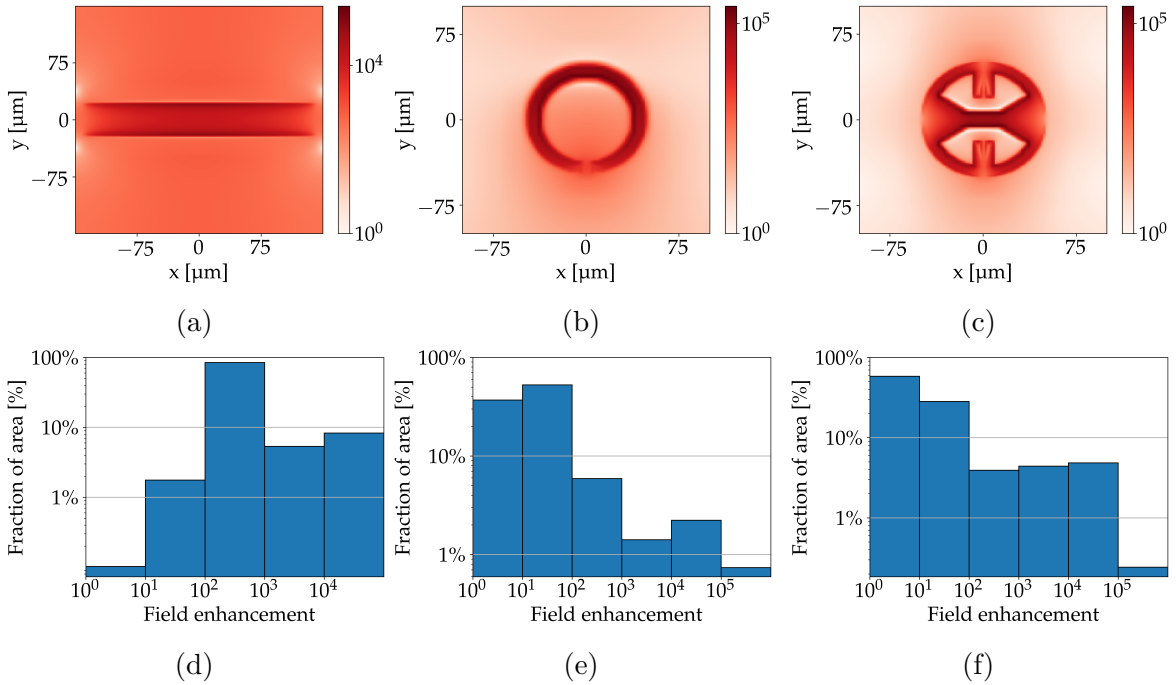


Figure 6.28: Local magnetic field enhancement in the vicinity of the antennas and corresponding histograms. (a, d) Bar antenna, (b, e) split ring and (c, f) split wheel. The maximum of each colour bar is set to $2.6 \cdot 10^5$, which corresponds to the maximum enhancement of the split wheel. Labels of the colour bar denote the order of magnitude of minimum and maximum enhancement for every map. Histograms show a fraction of the area where the local enhancement exceeds a given order of magnitude. Values were taken from an area of $300 \times 300\,\mu m^2$. $7 \times 7$ array of antennas was simulated in CST and data were taken for the middle antenna.

Now we compare the field distributions and the histograms for the middle antenna with data taken from the entire substrate. Figures 6.29–6.31 show local enhancement of in-plane magnetic field above entire substrate ($3000 \times 3000\,\mu m^2$). Each figure shows $7 \times 7$ array of particular antenna geometry. The field values were taken 0.4 µm above the substrate upper surface. To get the enhancement, the field values were divided by the reference field values of the source recorded at the same coordinates in simulation without the antennas.

The local enhancement maps and corresponding histograms show key differences between the bar antennas and the split ring or split wheel antennas again. Whereas the maximum enhancement of the bar antennas is an order of magnitude smaller, the enhancement in the area between them is very homogeneous and ranges from $10^1$ to $10^3$. This range contains almost 45 % of pixels. Just over 37 % of the area might be considered as an area having a neutral contribution since the values are between 1 and 10. This number is significantly higher than the per cent of pixels belonging to the same bin in Figure 6.28d, where we considered only the field values in the vicinity of the middle antenna. The majority of these pixels are near the edges of the substrate. Very high enhancement is present above the middle of each antenna. The map also shows an area where the field is strongly weakened.

As mentioned in the previous paragraph, the split ring and split wheel antennas produce very different field maps. Figures 6.30 and 6.31 show the local field enhancement maps and histograms analogous to the bar array. The field enhancement of these structures is much more confined. As the consequence, almost 90 % of the substrate area contains the field enhancement between 1 and 10. Less than 8 % of the area provides the enhancement between 10 and 100. Only 1 % of pixels possesses the enhancement value between $10^3$–$10^4$ and between $10^4$–$10^5$. Extreme values of the enhancement higher than $10^5$ are reached for only 0.001 % and 0.01 % of the substrate area for the split ring array and the split wheel array, respectively. This fraction corresponds to an area of approximately $100\,\mu m^2$ and $1000\,\mu m^2$.

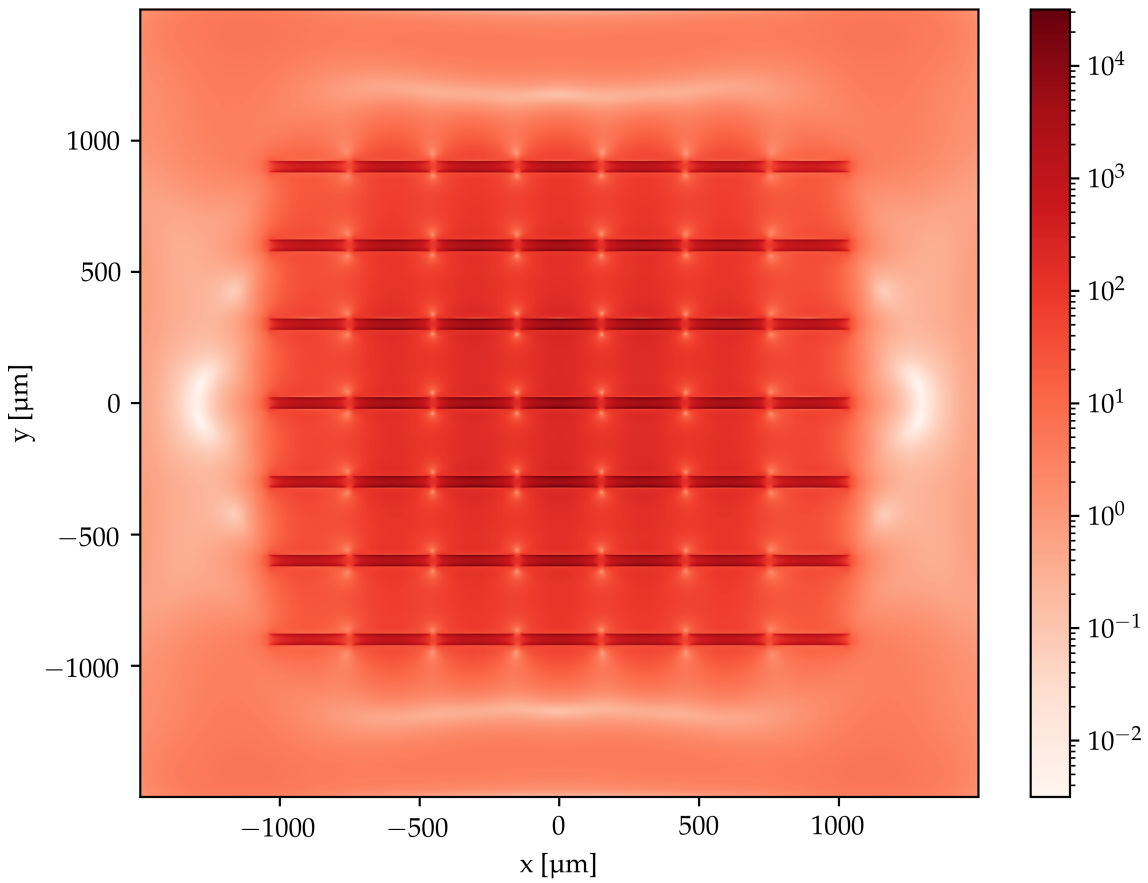


(a)

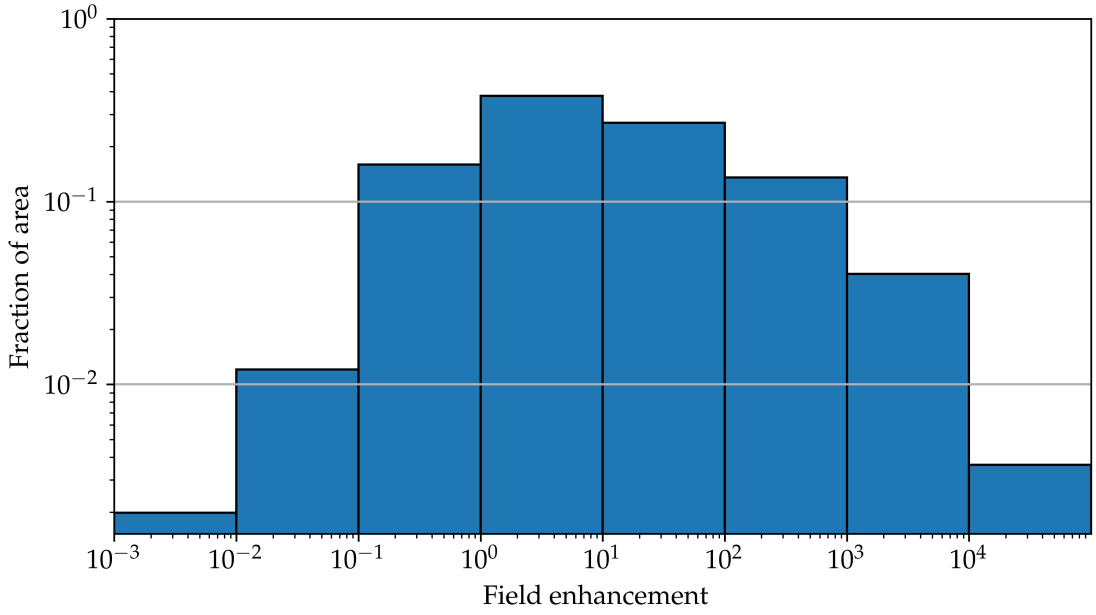


(b)

Figure 6.29: (a) Local magnetic field enhancement of the bar antennas. The field values were recorded 0.4 µm above surface of the substrate at the frequency of the LSP resonance (292 GHz). In-plane magnetic field values were divided by the source values point by point. (b) Histogram of the enhancement. Calculated in CST.

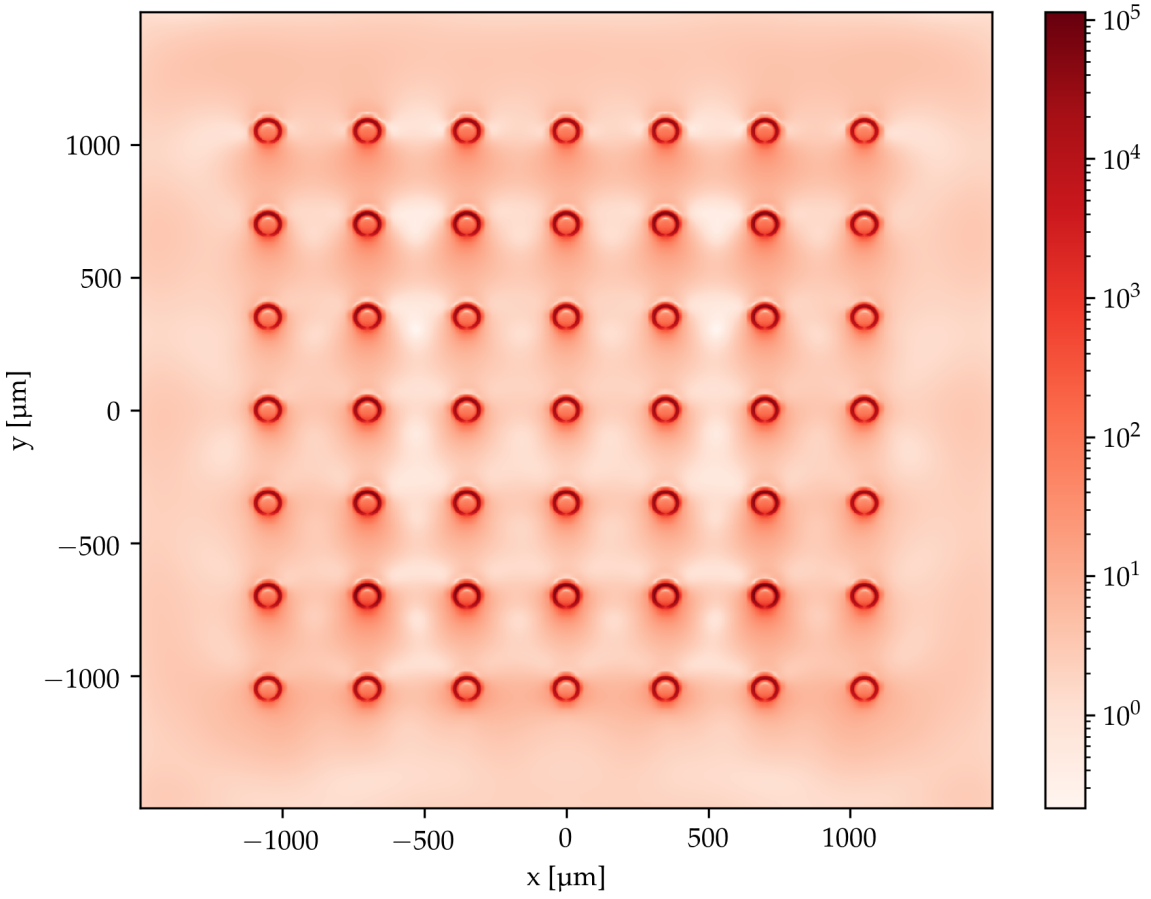


(a)

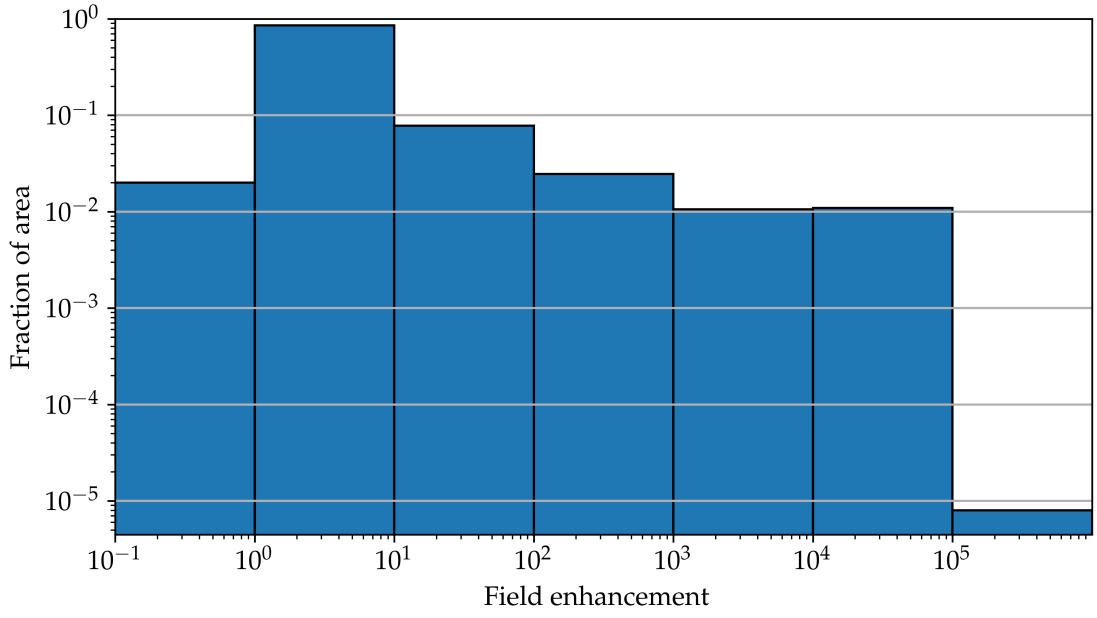


(b)

Figure 6.30: Local magnetic field enhancement of the split rings. The field values were recorded 0.4 µm above surface of the substrate at the frequency of the LSP resonance (309.5 GHz). In-plane magnetic field values were divided by the source values point by point. (b) Histogram of the enhancement. Calculated in CST.

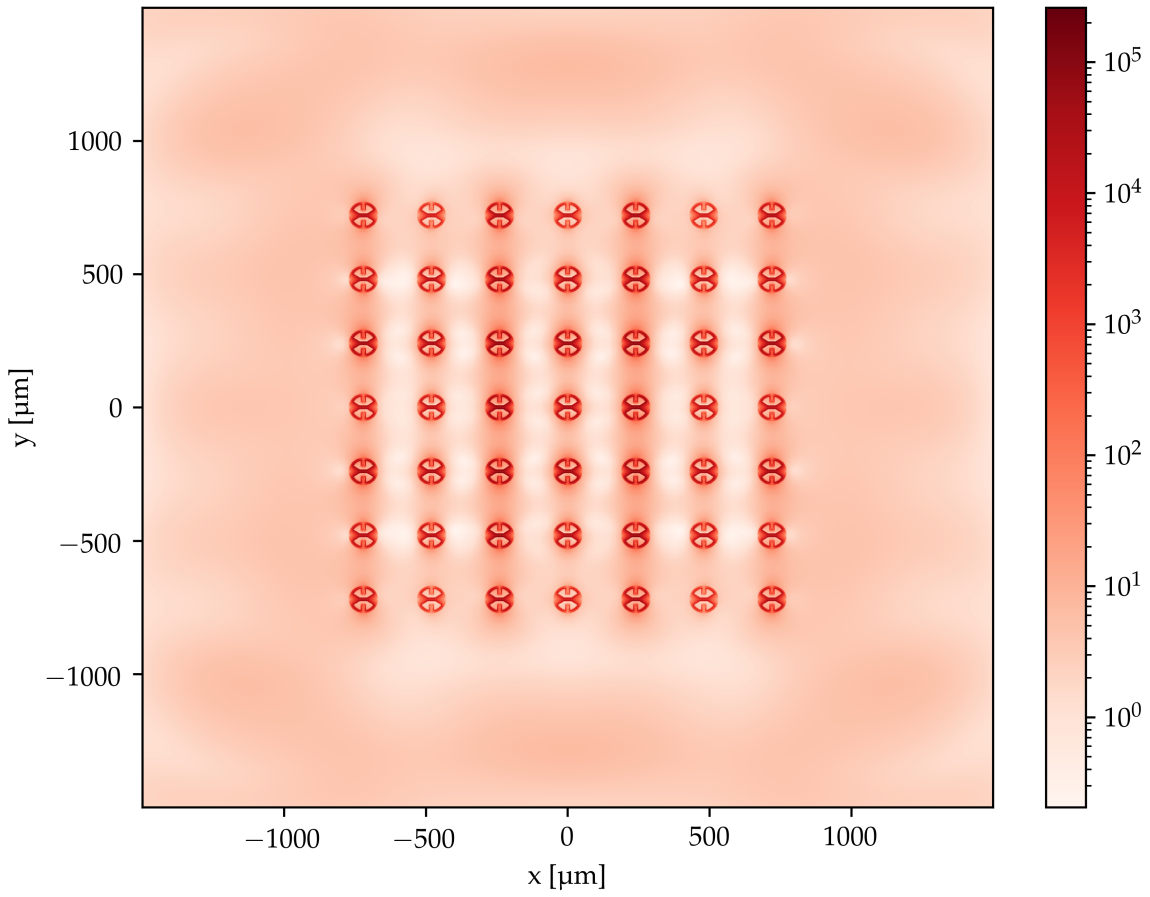


(a)

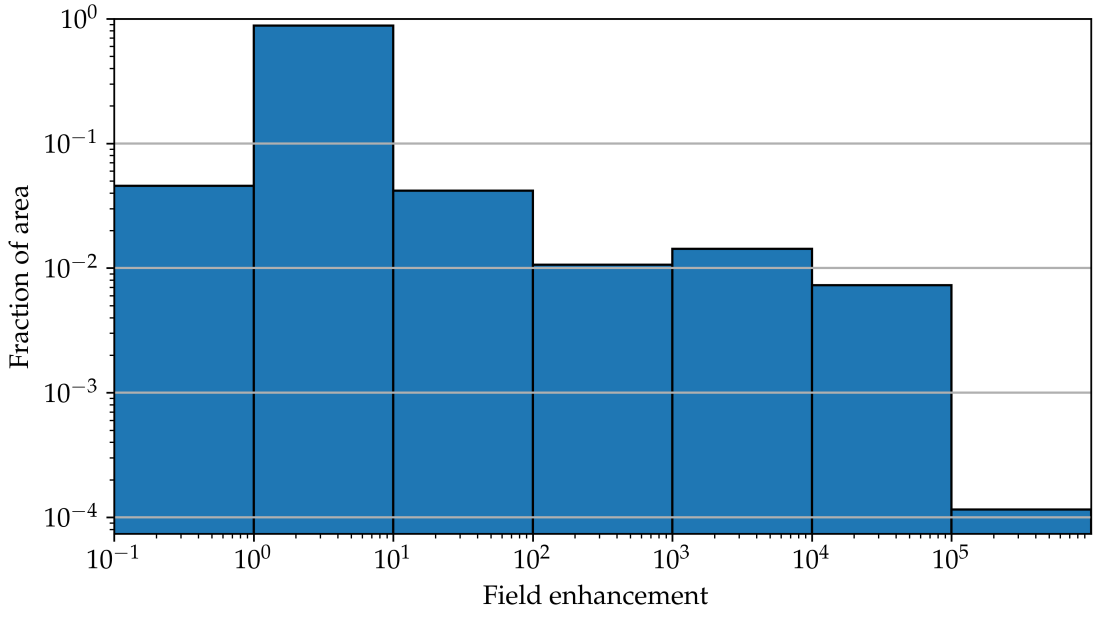


(b)

Figure 6.31: Local magnetic field enhancement of the split wheels. The field values were recorded 0.4 µm above surface of the substrate at the frequency of the LSP resonance (318 GHz). In-plane magnetic field values were divided by the source values point by point. (b) Histogram of the enhancement. Calculated in CST.

# Conclusions

The theory behind plasmonic antennas and their response to electromagnetic waves is very comprehensive and combines several fields of physics, including classical electromagnetic theory of light and solid state physics. Besides, the basics of computational electrodynamics and magnetism have to be taken into account. Dozens of books already cover these topics thoroughly. Therefore, the author summarizes only the fundamental theoretical background that is necessary for understanding the results of this work. The study of plasmonic antennas operating in the THz region and design of their shape suitable for enhancing the HFEPR signal were the main goals of this work.

Pursuing the first goal of the thesis, the author performed FDTD method based simulations of single plasmonic antennas in frequency region between 200 GHz and 400 GHz. The author used three different antenna geometries to show an average enhancement of the in-plane component of a magnetic field produced in the vicinity of them. To differentiate between various contribution to overall enhancement, the single antennas simulations were performed using an effectively semi-infinite substrate. The author clearly showed that the enhancement range of less than 10 times to more than 100 times. Low values of the enhancement were predicted for the bar antenna, which due to its simple geometry does not support any hotspot where the magnetic field could concentrate. In contrast, the split ring and the split wheel antennas were shown as an example of outstanding geometries enabling the concentration of the magnetic field. It resulted in the average enhancement exceeding 100. Subsequently, we have performed simulations with varied individual parameters. The author have identified the parameters that are critical for optimizing the enhancement in each of the antenna geometries in consideration. The cut-off angle $\theta$ improved the Q-factor of the split ring. In case of the split wheel structure, the enhancement is considerably improved by the capacitor-like rectangles. The split wheel structure was found as the most perspective. In addition, the author showed that simple relationship between the field enhancement and the Q-factor does not exist.

In the second part, the antenna arrays were studied extensively. The possibility of enhancing the signal of HFEPR spectrometer was probed and simulations were designed to be as close as possible to the real sample that is used in the real measurements. The author combined two types of simulation procedures. The first one was based on a semi-analytical approach and was used to calculate the response of effectively infinite arrays of antennas when taking into account finite thickness of the substrate and the presence of a gold mirror at the bottom side forming Fabry-Pérot resonator. It is shown that the resonator strongly affects the overall response of the system. Finally,

the second procedure simulated finite arrays of antennas on the substrate which follows all the real sample dimensions. The author numerically predicted the enhancement almost reaching three orders of magnitude for all simulated geometries. In contrast to the single antenna simulation, the author showed that average enhancement is rather independent of the antenna shape. However, the shape still plays an important role when creating the hotspots and it also significantly affects Q-factor. The Q-factor values higher than 200 have been achieved for the array of the bar antennas. These antennas also provide very homogeneous local field enhancement. It has been shown that the local enhancement in the vicinity of the bars is between 100 and 1,000. In contrast, the split ring and the split wheel antennas provide local enhancement exceeding 100,000 but only on the very small fraction of the substrate surface as the field is confined to sub-wavelength hotspots. Beside, the good agreement of CST simulations with simulations done using the semi-analytical ELM model opens new possibility to more extensive study of these antennas.

The results of the simulations presented in this thesis clearly show the possibility of enhancing the measured signal of HFEPR. A periodic arrangement of these antennas together with the Fabry-Pérot resonator is advantageous but single antenna based enhancement might be also possible.

# Bibliography


[1] LE, F. et al. Metallic nanoparticle arrays: a common substrate for both surface-enhanced Raman scattering and surface-enhanced infrared absorption. *ACS nano*. 2008, 2(4), s. 707–718. doi:10.1021/nn800047e.

[2] ANGER, P., P. BHARADWAJ a L. NOVOTNY. Enhancement and Quenching of Single-Molecule Fluorescence. *Phys. Rev. Lett.* 2006, (96), s. 113002. doi:10.1103/PhysRevLett.96.113002.

[3] MERTENS, H., A. F. KOENDERINK a A. POLMAN. Plasmon-enhanced luminescence near noble-metal nanospheres: Comparison of exact theory and an improved Gersten and Nitzan model. *Phys. Rev. B*. 2007, (76), s. 115123. doi:10.1103/PhysRevB.76.115123.

[4] SHEGAI, T. et al. Directional scattering and hydrogen sensing by bimetallic Pd-Au nanoantennas. *Nano letters*. 2012, 12(5), s. 2464–2469. doi:10.1021/nl300558h.

[5] TSENG, S.-C. et al. Eco-Friendly Plasmonic Sensors: Using the Photothermal Effect to Prepare Metal Nanoparticle-Containing Test Papers for Highly Sensitive Colorimetric Detection. *Analytical Chemistry*. 2012, 84(11), s. 5140–5145. doi:10.1021/ac300397h.

[6] SIEGEL, P. H. Terahertz technology. *IEEE Transactions on Microwave Theory and Techniques*. 2002, 50(3), s. 910–928. doi:10.1109/22.989974.

[7] DE MAAGT, P. a J. CHARLTON. Terahertz space applications and technology. 2005, s. 621–624, 2005. ISBN 0780388461.

[8] NEUGEBAUER, P. et al. Ultra-broadband EPR spectroscopy in field and frequency domains. *Phys. Chem. Chem. Phys.* 2018, (20), s. 15528–15534. doi:10.1039/C7CP07443C.

[9] CHATTOPADHYAY, G. Technology, Capabilities, and Performance of Low Power Terahertz Sources. *IEEE Transactions on Terahertz Science and Technology*. 2011, 1(1), s. 33–53. doi:10.1109/TTHZ.2011.2159561.

[10] MAIER, S. A. *Plasmonics: fundamentals and applications*. Springer, 2007. 223 s. ISBN 978-0-387-33150-8.

[11] HAMPSHIRE, D. A derivation of Maxwell's equations using the Heaviside notation. *arXiv.org*. 2018, 376. article ID number: 20170447.

[12] GRIFFITHS, D. J. *Introduction to electrodynamics*. Pearson new international edition, 2014, Fourth edition. 604 s. ISBN 978-1-292-02142-3.

[13] BORN, M. et al. *Principles of Optics: Electromagnetic Theory of Propagation, Interference and Diffraction of Light*. Cambridge University Press, 7, 1999. doi:10.1017/CBO9781139644181.

[14] JACKSON, J. D. *Classical electrodynamics*. John Wiley, 3rd ed., 1998. ISBN 0-471-30932-X.

[15] WEIL, J. A. J. A. *Electron paramagnetic resonance: elementary theory and practical applications*. John Wiley and Sons, 2nd ed., 2007. ISBN 978-0-471-75496-1.

[16] BLANK, A. et al. ESR imaging in solid phase down to sub-micron resolution: methodology and applications. *Phys. Chem. Chem. Phys.* 2009, (11), s. 6689–6699. doi:10.1039/B905943A.

[17] SMITH, G. et al. Quasi-optical cw mm-wave electron spin resonance spectrometer. *Review Of Scientific Instruments*. 1998, 69(11), s. 3924–3937. doi:10.1063/1.1149200.

[18] CROZIER, K. B. et al. Optical antennas: Resonators for local field enhancement. *Journal of Applied Physics*. 2003, 94(7), s. 4632–4642. doi:10.1063/1.1602956.

[19] SUNDARAMURTHY, A. et al. Field enhancement and gap-dependent resonance in a system of two opposing tip-to-tip Au nanotriangles. *Phys. Rev. B*. 2005, (72), s. 165409. doi:10.1103/PhysRevB.72.165409.

[20] SEOK, T. J. et al. Radiation engineering of optical antennas for maximum field enhancement. *Nano letters*. 2011, 11(7), s. 2606–2610. doi:10.1021/nl2010862.

[21] WEEBER, J.-C. et al. Plasmon polaritons of metallic nanowires for controlling submicron propagation of light. *Phys. Rev. B*. 1999, (60), s. 9061–9068. doi:10.1103/PhysRevB.60.9061.

[22] DRAINE, B. T. a P. J. FLATAU. Discrete-Dipole Approximation For Scattering Calculations. *J. Opt. Soc. Am. A*. 1994, 11(4), s. 1491–1499. doi:10.1364/JOSAA.11.001491.

[23] ROCKSTUHL, C., M. G. SALT a H. P. HERZIG. Application of the boundary-element method to the interaction of light with single and coupled metallic nanoparticles. *J. Opt. Soc. Am. A*. 2003, 20(10), s. 1969–1973. doi:10.1364/JOSAA.20.001969.

[24] PRATHER, D. W., M. S. MIROTZNIK a J. N. MAIT. Boundary integral methods applied to the analysis of diffractive optical elements. *J. Opt. Soc. Am. A*. 1997, 14(1), s. 34–43. doi:10.1364/JOSAA.14.000034.

[25] BRONGERSMA, M. a P. KIK. *Surface plasmon nanophotonics*. Springer, 2007, Springer series in optical sciences v. 131. ISBN 978-1-4020-4349-9.

[26] LEVEQUE, R. J. *Finite difference methods for ordinary and partial differential equations: steady-state and time-dependent problems*. Society for Industrial and Applied Mathematics, 2007. ISBN 978-0-89871-629-0.

[27] TAFLOVE, A. *Computational Electrodynamics: the finite-difference time-domain method*. Artech House, 1995. ISBN 0-89006-792-9.

[28] *FDTD product reference manual* [online]. 2003–2021. Available from: `https://support.lumerical.com/hc/en-us/articles/360033154434`.

[29] *CST MICROWAVE STUDIO user manual* [online]. 2014–2021. Available from: `https://manualzz.com/doc/28231181/cst-microwave-studio`.

[30] GOLDSMITH, P. F. *Quasioptical systems: Gaussian beam quasioptical propagation and applications*. IEEE Press, 1998, IEEE Press/Chapman and Hall Publishers series on microwave technology and RF. ISBN 0-7803-3439-6.

[31] CHEN, L. F. *Microwave electronics: measurement and materials characterization*. John Wiley and Sons, Ltd., 2004. ISBN 0-470-84492-2.

[32] ETCHEGOIN, P. G., E. C. LE RU a M. MEYER. An analytic model for the optical properties of gold. *The Journal of Chemical Physics*. 2006, 125(16), s. 164705. doi:10.1063/1.2360270.

[33] DERKACHOVA, A., K. KOLWAS a I. DEMCHENKO. Dielectric Function for Gold in Plasmonics Applications: Size Dependence of Plasmon Resonance Frequencies and Damping Rates for Nanospheres. *Plasmonics*. 2016, 11(3), s. 941–951. doi:10.1007/s11468-015-0128-7.

[34] PENDRY, J. B. et al. Magnetism from conductors and enhanced nonlinear phenomena. *IEEE Transactions on Microwave Theory and Techniques*. 1999, 47(11), s. 2075–2084. doi:10.1109/22.798002.

[35] KUMAR, N. et al. THz near-field Faraday imaging in hybrid metamaterials. *Optics Express*. 2012, (20), s. 11277–11287. doi:10.1364/OE.20.011277.

[36] TWIG, Y. et al. Note: High sensitivity pulsed electron spin resonance spectroscopy with induction detection. *Review of Scientific Instruments*. 2011, 82(7). doi:10.1063/1.3611003.

[37] KALOUSEK, R. et al. Response of plasmonic resonant nanorods: an analytical approach to optical antennas. *Opt. Express*. 2012, 20(16), s. 17916–17927. doi:10.1364/OE.20.017916.

[38] MIVELLE, M. et al. Strong Modification of Magnetic Dipole Emission through Diabolo Nanoantennas. *ACS Photonics*. 2015, 2(8), s. 1071–1076. doi:10.1021/acsphotonics.5b00128.

[39] GROSJEAN, T. et al. Diabolo Nanoantenna for Enhancing and Confining the Magnetic Optical Field. *Nano letters*. 2011, (11), s. 1009–13. doi:10.1021/nl103817f.

[40] SINGH, R., C. ROCKSTUHL a W. ZHANG. Strong influence of packing density in terahertz metamaterials. *Applied Physics Letters*. 2010, 97(24). doi:10.1063/1.3525169.

[41] ATAY, T., J.-H. SONG a A. NURMIKKO. Strongly interacting plasmon nanoparticle pairs: From dipole-dipole interaction to conductively coupled regime. *Nano Letters*. 2004, 4(9), s. 1627–1631. doi:10.1021/nl049215n.

[42] ROMERO, I. et al. Plasmons in nearly touching metallic nanoparticles: singular response in the limit of touching dimers. *Opt. Express*. 2006, 14(21), s. 9988–9999. doi:10.1364/OE.14.009988.